Elevated oxidized mercury in the free troposphere: Analytical advances and application at a remote continental mountaintop site

Eleanor J. Derry[1*], Tyler Elgiar[2‡], Taylor Y. Wilmot[3], Nicholas W. Hoch[1§], Noah S. Hirshorn[3+],
Peter Weiss-Penzias[4], Christopher F. Lee[5], John C. Lin[3], A. Gannet Hallar[6], Rainer Volkamer[5],
Seth N. Lyman[2,7], Lynne E. Gratz[1#]

[1]Environmental Studies Program, Colorado College, Colorado Springs, CO 80903 USA
[2]Bingham Research Center, Utah State University, Vernal, UT 84078 USA
[3]Department of Atmospheric Sciences, University of Utah, Salt Lake City, UT 84112 USA
[4]University of California, Santa Cruz, Santa Cruz, CA 95064 USA
[5]Department of Chemistry & CIRES, University of Colorado Boulder, Boulder, CO 80309 USA
[6]Storm Peak Laboratory, Department of Atmospheric Sciences, University of Utah, Salt Lake City, UT 84112 USA
[7]Department of Chemistry and Biochemistry, Utah State University, Logan, Utah, 84322 USA
[*]*Current affiliation:* Department of Chemistry, Reed College, Portland, OR 97202 USA
[‡]*Current affiliation:* Bureau of Land Management, Vernal, UT 84078 USA
[§]*Current affiliation:* BBA Water Consultants, Inc., Englewood, CO 80110 USA
[+]*Current affiliation:* Ramboll, New York, NY 10119 USA
[#]*Current affiliation:* Department of Chemistry and Environmental Studies Program, Reed College, Portland, OR 97202 USA

Correspondence to: Lynne E. Gratz (lgratz@reed.edu)

Abstract: Mercury (Hg) is a global atmospheric pollutant. In its oxidized form (Hg^{II}), it can readily deposit to ecosystems, where it may bioaccumulate and cause severe health effects. High Hg^{II} concentrations are reported in the free troposphere, but spatiotemporal data coverage is limited. Underestimation of Hg^{II} by commercially available measurement systems hinders quantification of Hg cycling and fate. During spring-summer 2021 and 2022, we measured elemental (Hg^0) and oxidized Hg using a calibrated dual-channel system alongside trace gases, aerosol properties, and meteorology at the high-elevation Storm Peak Laboratory (SPL) above Steamboat Springs, Colorado. Oxidized Hg concentrations displayed similar diel and episodic behavior to previous work at SPL, but were approximately three times higher in magnitude due to improved measurement accuracy. We identified 18 multi-day events of elevated Hg^{II} (mean enhancement: 36 pg m^{-3}) that occurred in dry air (mean ± s.d. RH = 32 ± 16%). Lagrangian particle dispersion model (HYSPLIT-STILT) 10-day back-trajectories showed that the majority of transport prior to events occurred in the low to mid-free troposphere. Oxidized Hg was anticorrelated with Hg^0 during events, with an average (± s.d.) slope of -0.39 ± 0.14. We posit that event Hg^{II} resulted from upwind oxidation followed by deposition or cloud uptake during transport. Meanwhile, sulfur dioxide measurements verified that three upwind coal-fired power plants did not influence ambient Hg at SPL. Principal Components Analysis showed Hg^{II} consistently inversely related with Hg^0 and generally not associated with combustion tracers, confirming oxidation in the clean, dry free troposphere as its primary origin.
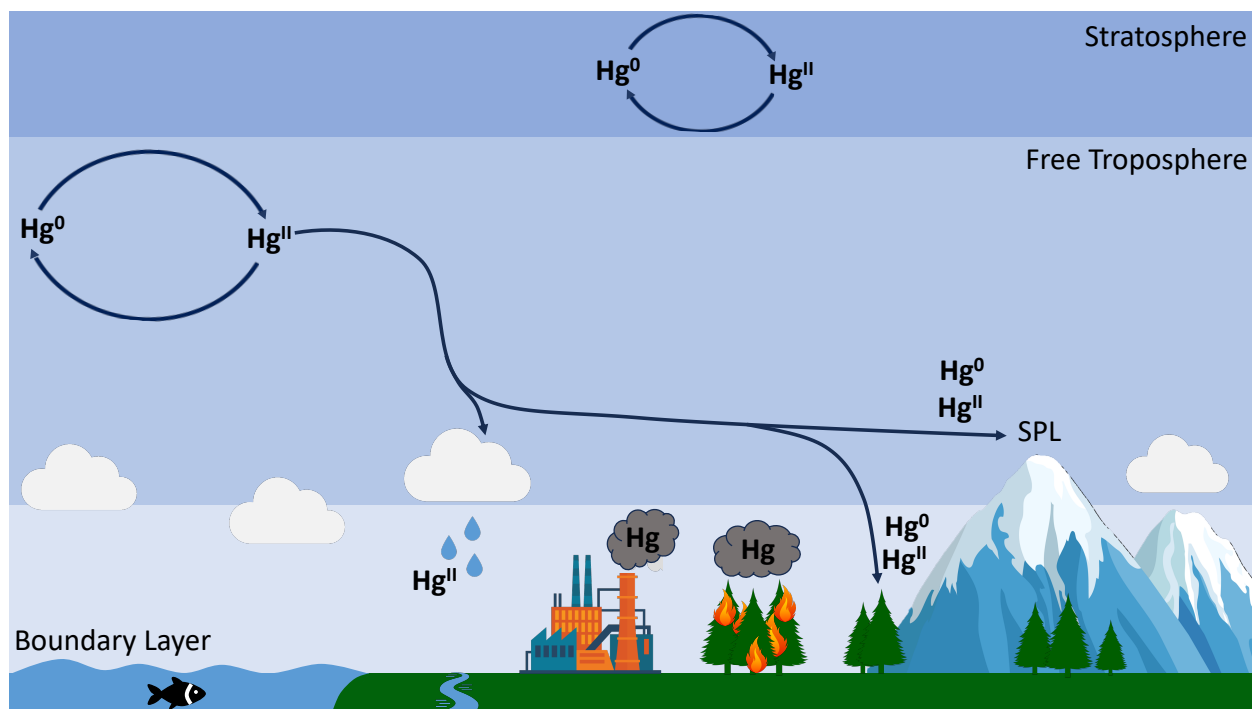
1. Introduction

Mercury (Hg) is a global pollutant that can be emitted to the atmosphere from both natural and anthropogenic sources. Humans have changed the Hg biogeochemical cycle through industrial development and land use practices that have increased atmospheric Hg concentrations and altered reservoir distributions (Obrist et al., 2018; Driscoll et al., 2013; Selin, 2009). Mercury is a toxin that can cause neurological and cardiovascular health effects depending on the duration, magnitude, and chemical form of exposure (Lyman et al., 2020a; Driscoll et al., 2013; Selin, 2009). In the atmosphere, Hg exists as gaseous elemental Hg (Hg^0; GEM), gaseous Hg^{II}–commonly referred to as GOM (gaseous oxidized mercury) or RGM (reactive gaseous mercury)–and particulate-bound mercury (PBM). Elemental Hg is relatively inert, and has an atmospheric lifetime on the scale of months (Bishop et al., 2020). Oxidized Hg (Hg^{II} = GOM + PBM), however, is much more reactive and water soluble, resulting in an atmospheric lifetime on the scale of days to a week in the planetary boundary layer (PBL) (Lyman et al., 2020a). Thus, when Hg^0 undergoes oxidation to form Hg^{II}, it is much more readily deposited into ecosystems, where it can methylate and bioaccumulate within food systems, with potential environmental and health consequences (Driscoll et al., 2013; Selin, 2009).

While international and domestic regulations have led to decreases in global background ambient Hg concentrations (Obrist et al., 2018; Lyman et al., 2020a), local conditions can vary significantly because of differences in the magnitude of urban and industrial emissions (Driscoll et al., 2013). Global background terrestrial Hg^0 concentrations also vary spatially; concentrations in the northern hemisphere reportedly range from 1.5 to 1.7 ng m^{-3}, and from 1.0 to 1.3 ng m^{-3} in the southern hemisphere (Sprovieri et al., 2016), caused by the higher concentration of urban areas and greater anthropogenic emissions in the Global North (Mao et al., 2016). Mercury

species have also been shown to exhibit variability with altitude. Elemental Hg is typically well mixed in the planetary boundary layer (PBL), while Hg^{II} has been shown to increase in concentration with elevation

60 (Swartzendruber et al., 2006; Faïn et al., 2009; Lyman and Jaffe, 2012; Gratz et al., 2015; Shah et al., 2016). The atmosphere is considered to be a minor reservoir of Hg (~5 GT) compared to soil (1,450 GT) and marine ecosystems (280 GT), but it is the dominant pathway for Hg inputs to ecosystems via deposition (Driscoll et al., 2013; Obrist et al., 2018; Lyman et al., 2020a). Oxidized Hg can be deposited via precipitation or dry deposition to both terrestrial and marine ecosystems. Recent work has posited that global models underestimate the importance of Hg^0 uptake by

65 vegetation and oceans, and are therefore biased toward Hg^{II} deposition (Sonke et al., 2023; Fu et al., 2021).

The chemical oxidation–reduction mechanisms of Hg in the atmosphere, which determine its environmental fate, are complex and not fully understood (Dibble et al., 2020; Lyman et al., 2020a; Shah et al., 2021; Castro et al., 2022). Previous studies have indicated multiple possible major oxidants of Hg in the atmosphere. While Hg oxidation can occur in the stratosphere, driven by a photosensitized oxidation mechanism (Saiz-Lopez et

70 al., 2022), as well as in both the marine and continental boundary layers (Lyman et al., 2020a), recent studies have suggested that Hg oxidation occurs primarily in the free troposphere, and the leading oxidants are halogens such as atomic bromine (Br) and the hydroxyl radical (OH) (Dibble et al., 2020). Oxidation in the free troposphere is thought to be driven by a two-step mechanism, in which ozone acts as a secondary oxidant (Shah et al., 2021; Castro et al., 2022). Previous studies have reported Br-initiated oxidation in the free troposphere (Gratz et al., 2015; Coburn

75 et al., 2016). A companion paper to this study further demonstrated that iodine-initiated oxidation may compete with Br- and OH-initiated oxidation at cold temperatures, and may be important to understanding the Hg oxidation mechanism (Lee et al., in review). This chemical cycling creates a pool of Hg^{II} within the free troposphere (Lyman and Jaffe, 2012; Shah et al., 2016; Weiss-Penzias et al., 2015).

Large uncertainties exist in the rate constants of the oxidation mechanism, and there remains a shortage of

80 experimental data (Castro et al., 2022). Part of this uncertainty comes from limitations in commercial instrument and measurement accuracy (Jaffe et al., 2014; Lyman et al., 2020b; Gustin et al., accepted). Most measurements of atmospheric Hg^{II} to date have relied on KCl-denuders, which exhibit a low bias (Lyman et al., 2020b and references therein). The extent of this low bias cannot be directly quantified, as most Hg^{II} measurements have been uncalibrated (Gustin et al., 2015; Jaffe et al., 2014). Thus, these datasets likely suffer from an underestimation of

85 atmospheric Hg^{II} concentrations (Lyman et al., 2020b).

Previous studies at mountaintop observatories in the U.S., Taiwan, and France have examined temporal trends in atmospheric Hg concentrations and consistently showed evidence of high concentrations of Hg^{II} in the clean, dry air of the free troposphere (Swartzendruber et al., 2006; Faïn et al., 2009; Sheu et al., 2010; Timonen et al., 2013; Fu et al., 2016). One such site is Storm Peak Laboratory (SPL), a high-elevation, continental research

90 station in the U.S. Rocky Mountains. Past work at SPL documented transitions between the PBL and the free troposphere using long-term measurements of aerosols and trace gases (Collaud Coen et al., 2018). Moreover, studies by Obrist et al. (2008) and Faïn et al. (2009) investigated the influence of anthropogenic Hg sources, as well as the effects of meteorology and air mass chemical composition on speciated Hg compounds. However, these and

other mountaintop studies historically relied on instrumentation that likely underestimated Hg^{II} concentrations (Lyman et al., 2020b).

In this study, we employed a calibrated Hg measurement technique with higher time resolution and improved measurement accuracy compared to other available methods (Lyman et al., 2020b; Elgiar et al., 2024). Data were collected at SPL above Steamboat Springs, Colorado during two six-month periods in spring and summer 2021 and 2022. We examined meteorology, air mass composition, and atmospheric transport during periods of elevated Hg^{II} to more accurately quantify the concentrations of Hg^{II} and to identify its origins in a continental atmosphere.

2. Methods

2.1 Site Description

The data used in this study were collected at Storm Peak Laboratory (3220 m AMSL; 40.455 N, 106.744 W) above Steamboat Springs, CO. SPL is a permanent high elevation research facility within the Rocky Mountains along the Continental Divide. The site is optimally located to characterize the remote continental atmosphere and transitions between the PBL and the free troposphere (Faïn et al., 2009; Collaud Coen et al., 2018). SPL receives prevailing westerly winds, creating a clear upwind fetch (Faïn et al., 2009). The site is located east of the agricultural Yampa Valley and approximately 19 km from downtown Steamboat Springs (Fig. A1). SPL is also located east and downwind of three coal-fired power plants, located in Hayden and Craig, CO and Vernal, UT, but otherwise sits in a relatively remote location with few nearby point sources that could influence atmospheric composition at the laboratory.

2.2 Data Collection

2.2.1 Dual-channel measurements of Hg^0 and Hg^{II}

The Utah State University (USU) dual-channel Hg measurement system operated at SPL from March 12, 2021 to October 11, 2021 and March 3, 2022 to September 22, 2022. The operation, validation, and quality assurance/control of this system at SPL are described in detail in Elgiar et al. (2024). Briefly, the dual-channel system pulls ambient air through the main Teflon-coated aluminum inlet at a rate of 9 standard L min^{-1} into a weatherproof box containing a thermal converter and a pair of in-series cation-exchange membranes. The thermal converter is constructed of quartz, packed with quartz chips, and maintained at a temperature of 650°C to convert Hg^{II} to Hg^0, such that total Hg is measured (THg = Hg^{II} + Hg^0) (Lyman et al., 2020b). The cation-exchange membranes remove Hg^{II} from the sample air stream, allowing only Hg^0 to pass through (Miller et al., 2019). A valve switches between the thermal converter and the cation-exchange membranes every five minutes. During each five-minute period, two 2.5-minute measurements are recorded by the downstream Tekran 2537X Hg^0 vapor analyzer. Oxidized Hg concentrations are computed as the difference between (a) two consecutive 2.5-minute THg measurements averaged together, and (b) the average of the 2.5-min Hg^0 measurement preceding and the one

following the consecutive THg measurements. As such, the system generates a complete set of Hg measurements (THg, Hg^0, Hg^{II}) every ten minutes. Inlet and sample lines are maintained at a temperature of 110°C to minimize contamination and wall losses.

130   Elemental mercury vapor injections on the Tekran 2537X were performed every 6 to 8 weeks using a Tekran 2505 calibration unit to verify the permeation rate of the internal calibration source. The soda lime trap upstream of the 2537X (used to prevent passivation of the internal gold traps) and the dual-channel's cation exchange membranes were replaced every two weeks, while the inlet was replaced every four weeks. The dual-channel system was also verified for measurement accuracy with an International System of Units (SI)-traceable

135   calibrator that injected known amounts of Hg^0, $HgBr_2$, and $HgCl_2$ into the inlet on a weekly basis, as described in Elgiar et al. (2024). All final Hg^0 and Hg^{II} concentrations were increased by 8% to account for a suspected bias in the Dumarey equation used for calculating vapor pressure of Hg^0 for manual injections (Elgiar et al., 2024; de Krom et al., 2021). One-hour average detection limits for Hg^{II} measurements were 12 ± 7 pg m^{-3} (mean $\pm$ 95% confidence interval of weekly detection limit tests conducted throughout the measurement season) in 2021 and 6 ± 2 pg m^{-3} in

140   2022. The detection limits were calculated as three-times the standard deviation of measurements of Hg^{II} during times when both channels were sampling Hg^{II}-free air. The percent standard uncertainty for Hg^0 and Hg^{II} with the dual-channel system, which takes into account the uncertainty budget for the Tekran 2537X analyzer (following the methodology of Brown et al. (2008)), and also for the performance of the dual-channel component of the system, was 8% (Elgiar et al., 2024). The placement of the dual-channel component of the system (e.g. the box containing

145   the thermal converter and cation exchange membranes) outdoors and immediately upstream of the inlet, as well as the development of an automated calibration system for Hg^0 and Hg^{II} compounds were both key improvements to the dual-channel system for the present study.

The dual-channel system may occasionally report negative values for Hg^{II} when the Hg^0 concentration is greater than the corresponding THg measurement used in the difference calculation (Dunham-Cheatham et al.,

150   2023). This may occur in plumes of rapidly changing concentrations, or for other reasons related to instrument performance that are as yet not fully understood. In this study, negative concentrations of hourly averaged Hg^{II} were computed only intermittently between May 2–11 2021, most notably during two approximately 24-hour periods between May 2 and May 4, and for approximately 10 hours on May 10. We therefore excluded several pairs of hourly averaged Hg^{II} and Hg^0 concentrations during this early May 2021 period (n = 65; 2% of the March 12 –

155   September 15, 2021 data). Removing these points did not change the 2021 mean, median, or standard deviation of Hg^0 within the measurement precision shown in Table 1; the spring 2021 mean $\pm$ s.d. decreased from 1.32 ± 0.10 to 1.31 ± 0.09 ng m^{-3}. For Hg^{II}, the exclusion of these values increased the 2021 mean $\pm$ s.d. from 101 ± 52 (median = 101) pg m^{-3} to 103 ± 49 (median = 102) pg m^{-3}, and increased the spring 2021 mean $\pm$ s.d. from 77 ± 54 (median = 67) pg m^{-3} to 82 ± 49 (median = 70) pg m^{-3}. In 2022, there was only one negative value for the hourly averaged Hg^{II}

160   concentrations, and that value along with the corresponding Hg^0 concentration were also removed. Other extended gaps in the datasets, related to instrument malfunction or operator error, included the periods from May 12 to June 6, June 29 to July 9, and August 2–10 in 2021, as well as June 27 to July 1 and August 16–23 in 2022.

Table 1: Summary statistics of Hg^0, Hg^{II}, trace gases, and aerosol PM$_1$ scattering (σ$_{sp}$) measurements by season and for each study year at SPL. The intermittent negative concentrations for Hg^{II} observed between May 2–11, 2021 (2% of hourly data) and one value in 2022 were excluded from the values reported in this table. See Sect. 2.2.1 for details.

		2021			2022		
		Spring	Summer	All	Spring	Summer	All
Hg^0	mean ± σ	1.31 ± 0.09	1.24 ± 0.14	1.27 ± 0.13	1.26 ± 0.12	1.25 ± 0.10	1.25 ± 0.11
(ng m^{-3})	median	1.34	1.25	1.30	1.29	1.25	1.27
	max	1.66	2.38	2.38	1.66	1.67	1.67
	N	1332	1727	3059	1718	2061	3779
Hg^{II}	mean ± σ	82 ± 49	120 ± 41	103 ± 49	80 ± 40	86 ± 29	83 ± 35
(pg m^{-3})	median	70	115	102	73	85	80
	max	520	253	520	239	197	239
	N	1323	1709	3032	1694	2053	3747
O$_3$	mean ± σ	48 ± 9	57 ± 8	53 ± 9	51 ± 6	53 ± 6	52 ± 6
(ppb)	median	50	57	54	51	53	52
	max	69	88	88	80	84	84
	N	1934	2473	4407	2208	2409	4617
NO$_x$	mean ± σ	1.9 ± 0.5	2.1 ± 0.7	2.1 ± 0.6	1.3 ± 1.0	1.3 ± 0.6	1.3 ± 0.8
(ppb)	median	1.9	2.0	1.9	1.0	1.2	1.1
	max	12	15	15	18	6.3	18
	N	1928	2473	4401	2207	2567	4774
SO$_2$	mean ± σ	0.0 ± 0.1	0.0 ± 0.2	0.0 ± 0.2	0.0 ± 0.3	0.0 ± 0.2	0.0 ± 0.2
(ppb)	median	0.0	0.0	0.0	0.0	0.0	0.0
	max	1.1	3.3	3.3	5.8	3.2	5.8
	N	1934	2540	4474	2195	2409	4604
CO	mean ± σ	NA	201 ± 94	NA	133 ± 20	123 ± 24	128 ± 23
(ppb)	median	NA	175	NA	134	121	128
	max	NA	1859	NA	211	276	276
	N	NA	1586	NA	2208	2568	4776
PM$_1$ σ$_{sp}$	mean ± σ	5 ± 3	55 ± 78	34 ± 64	4 ± 3	11 ± 10	7 ± 8
(Mm^{-1})	median	5	27	9	3	8	5
	max	17	816	816	33	164	164
	N	1849	2476	4325	2175	2460	4635

2.2.2 Criteria Gas and Meteorological Measurements

Several criteria gases and meteorological parameters were continuously measured at SPL related to this study. Meteorological data were measured on the roof of SPL at a height of 10 m above ground level (AGL) at a five-minute time resolution. Measured meteorological parameters included temperature, relative humidity (RH), wind speed and direction, and barometric pressure. These data were quality-assured and made publicly available by MesoWest (https://mesowest.utah.edu). We computed water vapor mixing ratios using a combination of measured temperature, RH, and barometric pressure, and the theoretical expression of the Clausius-Clapeyron equation.

Ozone (O$_3$), nitrogen oxides (NO$_x$), sulfur dioxide (SO$_2$), and aerosol properties such as scattering and absorption at 450, 550, and 700 nm were measured at a time resolution of one minute, and calibrated daily. Ozone was measured using a Thermo Model 49i Analyzer with a precision of 1.0 ppbv. Nitrogen oxides were measured

with a Thermo Model 42i NO-NO$_2$-NO$_x$ Analyzer with a precision of 0.2 ppbv. Sulfur dioxide was measured using

180   a Thermo Model 43i Analyzer with a precision of the greater value of either 1% or 1 ppbv. Aerosol properties were measured with a TSI model 3562 Nephelometer. Analysis for this manuscript relied on PM$_1$ scattering (PM$_1$ σ_{sp}) as the representative aerosol metric, in part for direct comparison with related studies (e.g. Timonen et al., 2013), and because the aerosol absorption data had more frequent gaps. Aerosol data were corrected to STP conditions and quality controlled/assured by NOAA ESRL GML (Andrews et al., 2019). Carbon monoxide (CO) was measured

185   beginning on July 7, 2021 with a Teledyne model 300E, from which average values were logged every 2.5 minutes in 2021 and every minute in 2022. The analyzer performed an automatic zero every 4 h in CO-free air; routine on-site spans for CO could not be performed due to COVID-19-related site access limitations, but based on those able to be performed before, during, and after the study, the measurement accuracy was estimated to be within ± 25%.

2.3 Data Analysis & Modeling Techniques

190   *2.3.1 Statistical Treatment of Data*

        The measurement data were averaged to one-hour intervals corresponding to the beginning of each hour to compare all the criteria on the same time step. Analyses in the present manuscript focus specifically on measurements made from March 13, 2021 to September 15, 2021 and from March 3, 2022 to September 15, 2022 to encompass two complete six-month periods each year. We defined spring as 1-March to 31-May and summer as 1-

195   June to 15-September given prior knowledge of the seasonal climatology and transport patterns (Obrist et al., 2008; Hallar et al., 2016). For example, past work has shown that trans-Pacific transport as well as stratospheric subsidence occur more commonly in springtime (Hallar et al., 2016), while summertime air masses at SPL are frequently impacted by biomass burning and different transport patterns (Obrist et al., 2018). Additionally, Hg concentrations have been shown to vary seasonally within the northern hemisphere, driven largely by seasonal

200   meteorology (Xu et al., 2022; Custódio et al., 2022).

        In this study, statistical significance was defined as $p < 0.05$. Reduced major axis (RMA) regressions were used to calculate linear regression slopes to account for uncertainty in both variables, as recommended for air quality data (Ayers, 2001). Correlation analysis was performed using Pearson's correlation coefficients (R), and comparisons of means were calculated using two-tailed independent sample t-tests and Mann-Whitney U tests.

205   Lastly, we estimated that at least one third of the ten-minute-averaged measurements in June – September 2021 showed evidence of smoke presence, whereas this was detected in less than 5% of data for the same timeframe in 2022. The presence of smoke was based on preliminary criteria of CO ≥ 150 ppbv, PM$_1$ σ_{sp} ≥ 30 Mm^{-1} and PM$_{10}$ σ_{sp} ≥ 35 Mm^{-1} for a minimum of one hour, and confirmation of overhead smoke using the National Oceanic and Atmospheric Administration Hazard Mapping System Fire and Smoke Product (NOAA HMS) (Air-Now Tech,

210   2023).

2.3.2 Identification of Events of Elevated Oxidized Mercury

Events of elevated Hg^{II} were initially defined as time periods when Hg^{II} concentrations exceeded the seasonal mean by at least one standard deviation (Table 1) for a minimum of 24 hours. Adjacent periods of elevated Hg^{II} were counted as the same event if they appeared to represent the same air mass, based on concurrent

215   meteorological and trace gas measurements (e.g., consistently similar Hg^0, Hg^{II}, and trace gas concentrations and RH before and after a brief intrusion of air associated with the boundary layer). Additional hours were then included in the events at the beginning and end of periods of high Hg^{II} in order to capture the transition between air mass conditions. In total, we identified 18 events of prolonged high Hg^{II} in the 2021 and 2022 measurement periods (Table 2). All events had at least 85% Hg data coverage. We characterized the events through statistical analysis of

220   Hg, trace gases, and meteorology as well as air mass transport analysis (Sect. 3.2.1 and 3.2.2) in order to understand the origins of the air masses containing elevated concentrations of Hg^{II}. We also analyzed the June 2022 measurement period as a case study because it contained relatively continuous records of all measured species and included five distinct events of high Hg^{II} (Events 11–15; Table 2), separated by periods of depleted Hg^{II} that were defined as non-events 1–5 (Sect 3.2.3). Non-Event 5 was made to include the 24 hours following the end of Event

225   15. Analysis of the measurement data within and between events was complemented by a simulation of air mass origins, as described below.

230

235

240   **Table 2: Event mean ± s.d. for Hg^{II}, Hg^0, RH, O_3, CO, and PM_1 σ_{sp}. [†]These events had evidence of smoke from local or regional biomass burning.**

Event	Date (MST)	Hg^0 (ng m^{-3})	Hg^{II} (pg m^{-3})	RH (%)	O_3 (ppb)	CO (ppb)	PM_1 σ_{sp} (Mm^{-1})
1	4/1/21 12:00 – 4/6/21 06:00	1.12 ± 0.07	137 ± 38	26 ± 8	40 ± 3	NA	4.5 ± 0.6
2	4/24/21 23:00 – 4/27/21 05:00	1.18 ± 0.06	121 ± 25	38 ± 16	53 ± 3	NA	5.0 ± 1.5
3	4/30/21 02:00 – 5/2/21 00:00	1.22 ± 0.06	115 ± 47	34 ± 7	51 ± 3	NA	2.6 ± 0.3
4	6/7/21 14:00 – 6/11/21 08:00[†]	1.03 ± 0.15	174 ± 52	20 ± 7	NA	NA	18.0 ± 21.4
5	6/13/21 23:00 – 6/15/21 21:00[†]	1.03 ± 0.09	156 ± 46	13 ± 4	49 ± 4	NA	20.3 ± 18.5
6	8/22/21 12:00 – 8/30/21 23:00[†]	1.08 ± 0.08	139 ± 31	36 ± 16	52 ± 5	150 ± 30	19.3 ± 21.6
7	9/6/21 05:00 – 9/11/21 05:00[†]	1.12 ± 0.07	173 ± 28	20 ± 7	63 ± 5	230 ± 50	49.5 ± 21.6
8	9/13/21 19:00 – 9/16/21 07:00[†]	1.29 ± 0.10	163 ± 32	35 ± 14	63 ± 6	160 ± 20	23.1 ± 9.7
9	5/10/22 00:00 – 5/12/22 15:00	1.09 ± 0.10	135 ± 50	35 ± 15	54 ± 5	120 ± 10	2.7 ± 0.8
10	5/25/22 19:00 – 5/27/22 18:00	1.13 ± 0.08	120 ± 34	39 ± 10	49 ± 3	110 ± 20	5.2 ± 1.2
11	6/3/22 04:00 – 6/5/22 04:00	1.08 ± 0.08	100 ± 21	38 ± 10	56 ± 3	110 ± 20	3.9 ± 1.1
12	6/7/22 00:00 – 6/11/22 17:00	1.18 ± 0.07	124 ± 19	38 ± 10	57 ± 7	130 ± 10	4.9 ± 1.4
13	6/12/22 18:00 – 6/13/22 23:00[†]	1.09 ± 0.10	117 ± 46	38 ± 30	55 ± 5	110 ± 40	21.3 ± 31.0
14	6/15/22 17:00 – 6/17/22 15:00[†]	1.12 ± 0.07	118 ± 13	28 ± 11	59 ± 7	130 ± 30	13.7 ± 10.0
15	6/20/22 07:00 – 6/23/22 02:00	1.12 ± 0.04	116 ± 20	30 ± 9	60 ± 5	120 ± 10	7.0 ± 3.6
16	7/20/22 07:00 – 7/22/22 23:00	1.21 ± 0.08	120 ± 12	35 ± 9	59 ± 3	120 ± 20	10.6 ± 2.2
17	7/25/22 00:00 – 7/27/22 23:00	1.21 ± 0.06	100 ± 30	49 ± 21	NA	140 ± 30	16.8 ± 5.8
18	9/11/22 18:00 – 9/13/22 23:00[†]	1.14 ± 0.05	107 ± 22	31 ± 25	55 ± 6	140 ± 20	26.9 ± 10.9

2.3.3 Air Mass Transport Analysis using HYSPLIT-STILT

The Hybrid Single-Particle Lagrangian Integrated Trajectory model integrating features from the Stochastic Time-Inverted Lagrangian Transport model (HYSPLIT-STILT) is a Lagrangian particle dispersion model (Loughner et al., 2021; Lin et al., 2003) that was used to investigate the history of air masses arriving at SPL. For each of the 18 events and 5 non-events presented here, an ensemble of 1,000 air parcels were released at SPL at three-hour intervals and traced for 240 hours backward in time. The air parcels were initialized at 5 m above ground level and transported with stochastic motions (simulating turbulence) with HYSPLIT-STILT, driven by meteorological fields from the 3 km meteorology from the High-Resolution Rapid Refresh model (HRRR; Dowell et al., 2022; NOAA ARL, 2024), as well as the 0.25°×0.25° meteorology from the Global Forecast System (GFS; NOAA ARL, 2024). Nesting HRRR meteorology within the relatively coarse GFS meteorological fields was necessary for simulating atmospheric transport over the Pacific Ocean. Along each air parcel's backward trajectory, position, the mixed layer depth, precipitation rate, RH, temperature, and total cloud cover from the meteorological fields were sampled at one-minute intervals, providing insight into the spatial origin and meteorological conditions associated with each air mass.

2.3.4 Principal Components Analysis

We used the Principal Components multivariate factor analysis technique (PCA) to investigate the interrelationships between measured variables and identify broad patterns in air mass composition at SPL. Factor analysis methods have been utilized in several studies involving continuous atmospheric measurements in both urban/industrial and remote environments (Swartzendruber et al., 2006; Liu et al., 2007; Lynam and Keeler, 2006; Tokarek et al., 2018). Other methods such as positive matrix factorization (PMF) or non-negative matrix factorization (NMF) are recommended for quantitative identification of source-receptor relationships (Hopke and Jaffe, 2020) and are often applied in urban/industrial environments using data from a common instrument (e.g. a suite of VOC measurements, as in Peng et al., 2022 and Gkatzelis et al., 2021). Though PCA is an unweighted least-squares method (Hopke and Jaffe, 2020), it has the advantage in the present study as an exploratory approach that can indicate both the magnitude and sign of the statistical relationships between variables (Jolliffe and Cadima, 2016). PCA is also advantageous at SPL where the combined dataset came from multiple continuous instruments with different measurement scales, and the objective was to use the underlying nature of statistical covariances to broadly characterize air mass compositions at SPL. PCA results were considered in tandem with the case study analysis to extrapolate the conditions under which enhancements in Hg^{II} or other variables were observed.

We applied PCA with Varimax rotation and Kaiser normalization (IBM SPSS v29.0.1.1) to each of the four sampled seasons in this study. Spring and summer were modeled separately, considering prior knowledge of seasonal climatology and transport (Obrist et al., 2008; Hallar et al., 2016), because air mass composition at SPL in summer 2021 was intermittently impacted by local or regional wildfire smoke (Sect. 2.3.1), and because the CO instrument was not operational in spring 2021. We additionally modeled the full 2022 measurement period (March 1

– September 15, 2022) because there was notably less evidence for regional wildfire smoke in the air at SPL during summer 2022.

Input variables for PCA included Hg^0, Hg^{II}, CO, O_3, NO_x, PM_1 σ_{sp}, water vapor mixing ratio, and barometric pressure. Wind speed was excluded given its weak communalities in the output for most seasons. Although Hg^{II} was generally better correlated with RH (Sect. 3.2.1), water vapor mixing ratio was used in place of RH in PCA as a potentially better indicator of atmospheric moisture content, and because the upper bound of 100% in RH measurements influences its statistical distribution. Moreover, after filtering the data for RH < 85% to exclude periods when SPL may have been in cloud, the Pearson's R and p-values for Hg^{II} vs. water vapor mixing in each season did not substantially change in comparison to Hg^{II} vs. RH, indicating that water vapor mixing ratio was a robust predictor of Hg^{II} even if not as strong as RH (Table A1). Sulfur dioxide was excluded because it was near 0 ppbv on average (Table 1), with enhancements observed only in short-lived fresh combustion plumes.

Prior to running PCA, variables with |skewness| larger than 0.5 (moderate skew) or larger than 1.0 (high skew) were log-transformed. If the |skewness| did not improve then the non-log-transformed variable was retained. All variables with |skewness| > 1.0 improved following log transform. In most seasons, PM_1 σ_{sp} also needed to be shifted by its minimum before transformation due to small negative values. Data points three standard deviations above or below the dataset mean were then removed as outliers (< 2% of values for each variable). Lastly, variables were standardized (mean = 0, standard deviation = 1) by subtracting that variable's mean and dividing by the standard deviation for the sample period. Data were excluded listwise by the model, meaning all data for a given hourly timestamp were removed from the model if one or more variables had no data. This technique ensured that there were no missing data in the input dataset, but reduced the total number of timestamps in included in each input dataset by 40% in spring 2021 (n = 1169), 55% in summer 2021 (n = 1147), 29% in spring 2022 (n = 1575), 33% in summer 2022 (n = 1729), and 31% in spring–summer 2022 (n = 3299). The larger percent reductions during 2021 reflect the delayed start of CO measurements and several prolonged maintenance periods; nevertheless, there were ample cases per variable to confirm data suitability for PCA.

Suitable solutions were identified using the Kaiser–Meyer–Olkin (KMO) measure of sampling adequacy for the overall dataset and for individual variables (preferring outputs with KMO > 0.5), and Bartlett's test of sphericity (p < 0.05). Individual variables were also considered for inclusion in the final solution based on extraction communalities > 0.5. The final number of factors was chosen based on the eigenvalue > 1 criteria.

3. Results and Discussion

3.1 Data Overview

3.1.1 Mercury Overview

Figure 1 and Table 1 summarize the hourly-averaged measurements of Hg and trace gases from the 2021 and 2022 periods. Overall, mean Hg^0 concentrations varied minimally from 2021 (1.27 ± 0.13 ng m^{-3}) to 2022 (1.25 ± 0.11 ng m^{-3}), from spring to summer in each year, or from one season to that same season in the following year,

even though t-tests for comparisons of seasonal means all indicated statistically significant differences ($p < 0.01$). The largest mean difference in Hg^0 was from spring to summer 2021, but was still less than a 0.1 ng m^{-3} change. Mean Hg^{II} concentrations were not significantly different between the two spring seasons ($p = 0.33$), whereas the summer 2021 mean was significantly higher ($p \ll 0.001$) than in summer 2022.

Figure 1: Time series of hourly-averaged concentrations of Hg^0 (blue) and Hg^{II} (red) in units of ng m^{-3} between March 1 and September 15 of 2021 and 2022, as measured by the dual-channel system at Storm Peak Laboratory above Steamboat Springs, CO.

3.1.2 Trace Gas Overview

Mean values of O_3, NO_x, CO, and aerosol scattering were significantly different ($p < 0.01$) between the two spring seasons (excluding CO, which was not available in spring 2021) and between the two summer seasons (Table 1). Mean values were also significantly different between each spring season and the corresponding summer from that year with the exception of NO_x in 2022 ($p = 0.52$). It was notable that O_3 displayed a relatively flat diel pattern, with mean diel amplitudes of only 4 ppbv in both spring seasons and 2–3 ppbv in the summer seasons, lacking the pronounced daytime enhancement that is commonly seen at lower elevation sites (Fig. A2). This behavior was similar to what has been reported at other high elevation sites that were less influenced by daytime production from local precursor emissions or by nighttime loss processes in the presence of NO_x sources (Mueller, 1994; Monks et al., 2000; Bien and Helmig, 2018; Brodin et al., 2010), suggesting that SPL was routinely influenced by the background free troposphere even in the summertime. Higher mean concentrations of O_3, NO_x, CO, and aerosol scattering in summer 2021 compared to 2022 may be related, at least in part, to observed differences in the frequency of wildfire smoke presence (Sect. 2.3.1).

We also considered the potential influence of the three upwind coal-fired power plants, located 40, 80, and 200 km west of SPL, on Hg concentrations measured at SPL. These plants were shown to influence air mass composition at SPL through emissions of SO_2 that can contribute to new particle formation (Hallar et al., 2016). A goal was to determine whether elevated Hg^0 or Hg^{II} concentrations occurred primarily in the background atmosphere or also under the influence of local or regional point-source emissions. Air masses at SPL were initially defined as power plant-impacted using the 95th percentile of 10-minute averaged SO_2 concentrations from the 2021 measurement period. We then examined local wind speed and direction measurements at SPL along with 24 hour HYSPLIT back trajectories. We also considered several case studies of the highest SO_2 concentrations in each season. Together, these observations showed that higher concentrations of SO_2 reliably corresponded to a westerly source region representative of the three upwind power plants. Smoke-impacted periods (Sect. 2.3.1) were excluded from this analysis.

Mean Hg^0 and Hg^{II} concentrations in spring were statistically significantly different between power plant-impacted and non-impacted air masses; however, the differences were small enough that we did not consider them to be detectable within instrument precision (Δ mean Hg^0 = -0.02 ng m^{-3}, Δ mean Hg^{II} = +4 pg m^{-3}). Differences in summertime measurements of Hg^0 and Hg^{II} between the two types of air masses were also statistically significantly different but only slightly elevated in power plant-impacted air masses (Δ mean: Hg^0 = +0.04 ng m^{-3}, Hg^{II} = +12 pg m^{-3}). Yet, the coefficients of determination between Hg^0 and SO_2 as well as Hg^{II} and SO_2 within power plant-impacted periods were very low in both spring and summer (R^2 = 0.00 – 0.03) indicating that little to no variation in Hg species could be explained by the variability in SO_2. We therefore concluded that the three coal-fired power plants upwind of SPL did not significantly contribute to ambient Hg measurements made at SPL. The lack of a measurable enhancement in Hg at the lab when the coal-fired power plant signature was evident can likely be attributed to power plant emissions controls and lower Hg content coal (Benson, 2003).

3.1.3 Comparison to Similar Studies

Mean Hg^0 concentrations in this study (1.27 $\pm$ 0.13 ng m^{-3} in 2021 and 1.25 $\pm$ 0.11 ng m^{-3} in 2022) were lower than those reported at other remote mountaintop observatories between 2005–2016, including the Mt. Bachelor Observatory (MBO) in central Oregon, USA (1.54 $\pm$ 0.176 ng m^{-3} from May – August 2005; Swartzendruber et al., 2006), the Lulin Atmospheric Background Station (1.73 ng m^{-3} from April 2006 to December 2007; Sheu et al., 2010), the Pic du Midi Observatory in southern France (1.86 $\pm$ 0.27 ng m^{-3} from November 2011 – November 2012; Fu et al., 2016), and previously at SPL (1.51 $\pm$ 0.11 ng m^{-3} from October 2006 – May 2007 (Obrist et al., 2008); 1.6 $\pm$ 0.3 ng m^{-3} from April – July 2008 (Faïn et al., 2009)). The observed Hg^0 means at SPL in 2021 and 2022 were also lower than estimated global background concentrations in the northern hemisphere (1.5–1.7 ng m^{-3}; Sprovieri et al., 2016; Mao et al., 2016). One plausible explanation for these differences is the reported declines in ambient Hg^0 concentrations in the northern hemisphere from the 1990s to 2005–2013, albeit the magnitudes of reported trends are variable from region to region, ranging from less than 1% to as much as 3.3% per year in northern latitude sites (Lyman et al., 2020a and references therein). Meanwhile Slemr et al. (2011) estimated decreasing trends from 1996 to 2009 of -0.047 ng m^{-3} y^{-1} (1.4% per year) and -0.035 $\pm$ 0.006 ng m^{-3} y^{-1} (2.7% per

year) for the northern and southern hemispheres, respectively. Weigelt et al. (2015) reported a decline of 0.021–

0.023 ng m^{-3} y^{-1} in THg from 1996 to 2013 at the Global Atmospheric Watch (GAW) station in Mace Head, Ireland,

370   one of the longest running Hg background measurement stations in the northern hemisphere. Since the mid-2000s,

some studies have reported more modest decreases or even increases in some locations, attributed to variable

anthropogenic emission trends and biomass burning, changes in Hg cycling and exchange rates, and the effects of

temperature on deposition rates (Lyman et al., 2020a and references therein). There remains considerable

uncertainty and inconsistency in analyses of atmospheric Hg trends, largely because of incomplete emission

375   inventories, and a lack of both spatial and long-term measurement coverage (Sonke et al., 2023; Lyman et al.,

2020a).

Keeping these spatiotemporal trends and sources of uncertainty in mind, we compared the mean Hg^0

concentrations at SPL from Obrist et al. (2008) and Faïn et al. (2009) (~1.56 ng m^{-3}) with the mean Hg^0 at SPL in

2021 and 2022 (~1.26 ng m^{-3}). Considering this drop of ~0.3 ng m^{-3} over 14 years, it can be estimated that the more

380   recent measurements were lower by 0.021 ng m^{-3} y^{-1} (~1.4% per year) values that are within the range of reported

downward trends in northern hemisphere background concentrations (Slemr et al., 2011; Weigelt et al., 2015;

Lyman et al., 2020a; Sonke et al., 2023). Such a difference could also be related to changes in measurement

technology between earlier studies and the present one, i.e. gaseous Hg^{II} (aka, RGM or GOM) that was not retained

on the KCl denuder in the earlier SPL studies may have instead been captured downstream as Hg^0 resulting in an

385   overestimate of Hg^0 concentrations (Lyman et al., 2010). Even so, total Hg would still have been conserved; yet, the

mean (± 1 s.d.) concentrations of THg were only 1.37 ± 0.11 and 1.34 ± 0.09 ng m^{-3} in in 2021 and 2022,

respectively, suggesting that SPL may in fact have experienced declining ambient Hg concentrations over time.

In contrast, concentrations of Hg^{II} measured with the dual-channel measurement system in 2021 (103 ± 49

pg m^{-3}) and 2022 (83 ± 35 pg m^{-3}) (Table 1) were considerably higher than the previous measurements made at SPL

390   using the KCl-denuder system (Faïn et al., 2009). Summing the April – July 2008 mean measurements of GOM (20

pg m^{-3}) and PBM (9 pg m^{-3}) in Faïn et al. (2009), it can be estimated that the mean Hg^{II} during that study period was

29 pg m^{-3}, which is lower than the spring-summer means in 2021 and 2022 by 3.6- and 2.8-times, respectively. The

maximum GOM+PBM concentration Faïn et al. (2009) recorded during GOM enhancement events was 159 pg m^{-3}

(Event 4), which is 3.3 times lower than the 2021 maximum (520 pg m^{-3}) and 1.5 times lower than the 2022

395   maximum (239 pg m^{-3}). Relatedly, mean measurements of GOM and PBM at other mountaintop sites using the KCl

denuder system were respectively 43 pg m^{-3} and 5.2 pg m^{-3} (MBO, USA; Swartzendruber et al., 2006), 12.1 pg m^{-3}

and 2.3 pg m^{-3} (LABS, Taiwan; Sheu et al., 2010), and 27 pg m^{-3} and 14 pg m^{-3} (PDM, France; Fu et al., 2016).

While these sites occasionally saw large spikes on the order of hundreds of pg m^{-3}, it is particularly striking that

mean Hg^{II} concentrations in the present study were consistently higher than these other sites by a factor of roughly 2

400   to 5. These observations have important implications for the accurate representation of total Hg speciation in

ambient air. For example, estimates of the fraction of atmospheric THg composed of gaseous Hg^{II} have ranged from

2–20% depending on sampling location and instrumentation (Dunham-Cheatham et al., 2023; Gustin et al., 2023;

Osterwalder et al., 2021; Steffen et al., 2008) During events of elevated Hg^{II} in the present study (Sect 3.2), the

maximum percent Hg^{II} of THg ranged from 12–22%, with a mean (± s.d.) of 11 ± 2%. Comparatively, the previous

405 study at SPL using KCl denuders had a mean Hg^{II}:THg ratio during enhanced RGM events of approximately 3 ± 1% (Faïn et al., 2009). The recent measurements at SPL using the dual-channel system thus represent a significant contribution to the research field in the ability to report verified, accurate, and reliably higher Hg^{II} concentration measurements than in past studies.

In both years, and for all sampled seasons, Hg^0 did not display a pronounced diel pattern (Fig. 2).
410 Concentrations generally displayed higher concentrations throughout the day in spring 2021 compared to the same hours in summer 2021 and spring 2022, whereas the spread of data at each hour was larger in summer 2021 and spring 2022. Nevertheless, the diel curves were relatively flat across the hours within all sampled seasons. This finding is in contrast to previous work by Obrist et al. (2008) at SPL, who reported a distinct springtime diel pattern for Hg^0. Oxidized Hg, however, displayed markedly higher concentrations during the spring daytime (Fig. 2), with
415 maxima centered around 11:00–12:00 MST and mean diel amplitudes of 58 pg m^{-3} in spring 2021 and 32 pg m^{-3} in spring 2022. On a monthly basis (not shown), daytime enhancements were the most pronounced in March 2021 with a mean diel amplitude of 117 pg m^{-3}. In both years, this pattern diminished throughout the spring and into the summer of 2021, with mean diel summer amplitudes of 16 pg m^{-3} (2021) and 19 pg m^{-3} (2022). The diel curves for Hg^{II} also emphasize the overall higher concentrations measured throughout all hours of the day in summer 2021,
420 particularly overnight, as compared to summer 2022 (Fig. 2, Table 1).
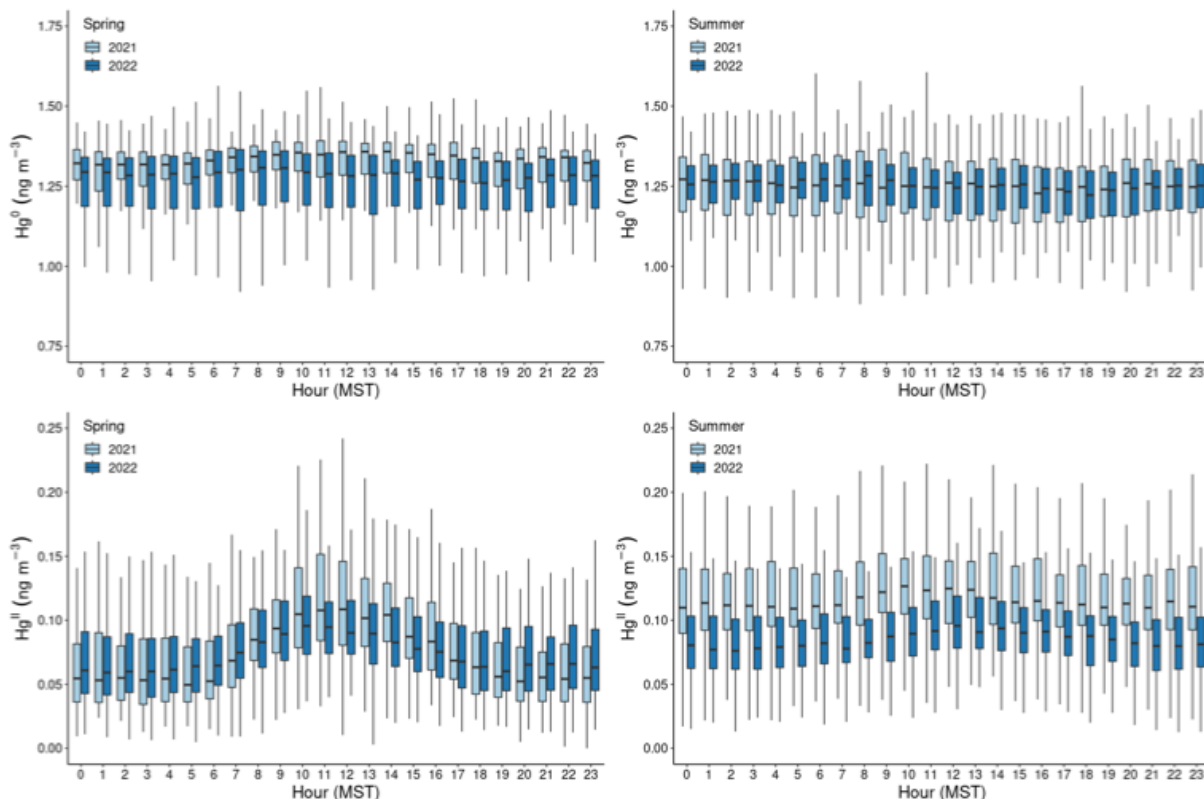
Figure 2: Boxplots of concentration measurements by hour of day (MST) for Hg^0 (top) and Hg^{II} (bottom), showing diel variability during the spring (left) and summer (right) seasons of the study years. The centerline of each boxplot represents the median concentration, the box represents the interquartile range, and

upper/lower whiskers are either the maximum/minimum value or the upper/lower quartile value plus/minus 1.5 times the interquartile range. Outliers are not shown.

Higher daytime concentrations of Hg^{II} were also observed at SPL by Faïn et al. (2009). The authors attributed this behavior to surface heating processes and uplift of boundary layer air; however, the daytime maxima during that study tended to occur later in the day, closer to 15:00 MST. In both 2021 and 20222, aerosol PM_1 scattering also peaked at midday in spring (Fig. A2) but the amplitude of this enhancement was very small (0.9–2.3 Mm^{-1}). Aerosol PM_1 scattering was significantly correlated with Hg^{II} in spring 2021, when the daytime enhancement was strongest ($R^2 = 0.30$). These factors could indicate that upslope pollution flow from the local boundary layer contributed to elevated daytime Hg^{II} or that the elevated Hg^{II} was due to the breakup of the polluted nighttime boundary layer in the Yampa Valley and transport of its pollutants to the site. However, SO_2, NO_x, O_3, and water vapor mixing ratio did not show a notable peak in daytime that would support the notion of transport or mixing from the local boundary layer. If the source of daytime Hg^{II} was the breakup of the polluted Yampa Valley boundary layer, it is also not clear why only Hg^{II}, and not Hg^0, was elevated. In many other studies, urban pollution is associated with Hg^0, and not just Hg^{II} pollution (Driscoll et al., 2013).The cause of the early spring daytime Hg^{II} maximum at SPL thus remains an open question.

The lack of diel variability in Hg^0 and a daytime peak in Hg^{II} seen in present and past work at SPL is in contrast to other mountaintop studies which reported higher Hg^{II} overnight and in the early morning hours, typically attributed a shallow planetary boundary layer and subsidence of Hg^{II}-rich air from the upper troposphere and lower stratosphere (UT/LS) (Swartzendruber et al., 2006; Sheu et al., 2010; Fu et al., 2016). Nighttime subsidence of Hg^{II} from the UT/LS at MBO, PDM, and LABS was also supported by observations of lower RH, higher ozone, and air mass back-trajectories pointing to upper tropospheric transport. Further analysis at MBO also identified episodes of high Hg^{II} with transport from the marine boundary layer or trans-Pacific transport of combustion emissions from East Asia (Timonen et al., 2013). The more continental nature of SPL is one likely factor that contributed to the different features and transport pathways associated with high Hg^{II} than these other mountaintop sites, as any air masses influenced by the marine boundary layer or trans-Pacific sources may have been diluted by regional continental air masses before reaching the site. Faïn et al. (2009) also showed, and we confirmed in the present work (Sect. 3.2), that high Hg^{II} events at SPL were not associated with UT/LS subsidence and were instead influenced by transport from within the low to mid-free troposphere, at least in the 10 days of simulated transport history.

3.2 Multi-day events of enhanced Hg^{II}

3.2.1 Behaviors in Hg^0, Hg^{II}, and atmospheric transport

Based on the criteria described in Sect. 2.3.2, we identified 18 events of enhanced Hg^{II} during the 2021 and 2022 measurement periods. Three events occurred during spring 2021, five during summer 2021, two during spring 2022, and eight during summer 2022 (Table 2). Across all events, elevated Hg^{II} concentrations were associated with concurrent decreases in Hg^0 and RH (Fig. 3). Relative humidity was consistently low during the event periods, with a mean ($\pm$ s.d.) event RH of $32 \pm 16\%$. This observation of high Hg^{II} in very dry air masses is consistent with the

460   results of Faïn et al. (2009), who concluded that Hg^{II} enhancements at SPL were associated with air masses in the

dry (RH < 40%) free troposphere. In all but Event 10, Hg^{II} was significantly anticorrelated with Hg^0 (Pearson's R =

-0.95 to -0.41, p < 0.001), and in all but Event 14, Hg^{II} was significantly anticorrelated with RH (Pearson's R = -

0.81 to -0.28, p < 0.05). Similar to Faïn et al. (2009), Hg^{II} was also anticorrelated with water vapor mixing ratio

during 12 events (Pearson's R = -0.74 to -0.12, p < 0.05). RMA regression slopes (± standard error) for Hg^{II} versus

465   Hg^0 during each event ranged from -0.76 ± 0.01 to -0.16 ± 0.01 (Table 3), with an average event slope (± s.d.) of -

0.39 ± 0.14. Though previous work at SPL also showed negative RGM versus GEM slopes during high RGM

events, the magnitudes were only between -0.07 to -0.18, with an average of -0.10 (Faïn et al., 2009). This

difference likely reflects, at least in part, the improved accuracy of the dual-channel system in measuring Hg^{II} than

previously used instrumentation (Sect. 3.1). The slope of all hourly data during event periods (± standard error) in

470   2021 and 2022 was -0.38 ± 0.09 (Fig. 3).
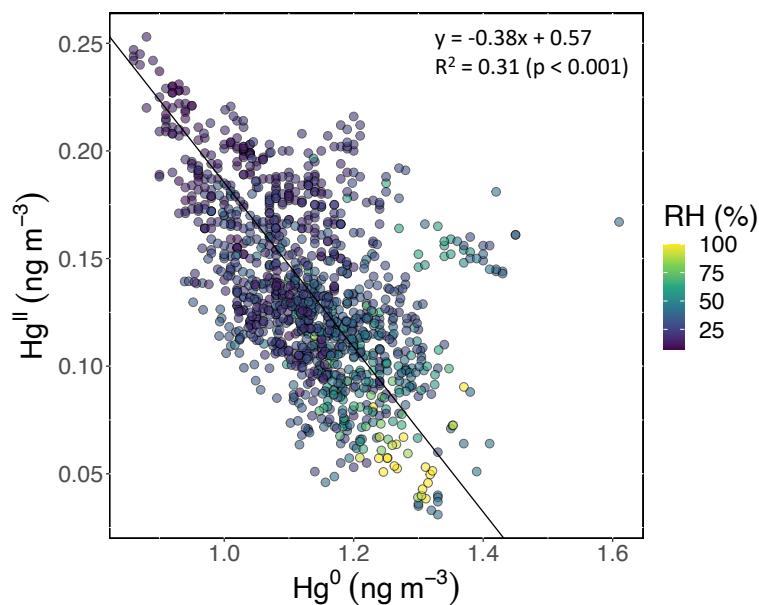
Figure 3: Hg^{II} vs Hg^0 for hourly measurements during all 18 events, color coded by RH. Hg^{II} was significantly
anticorrelated with Hg^0 (Pearson's R = -0.55, p << 0.001) and RH (Pearson's R = -0.56, p << 0.001). The slope
of the RMA regression (± S.E.) was -0.38 ± 0.09, which is similar to the average of all 18 event slopes (± s.d.),
475   **which was -0.39 ± 0.14.**

480

Table 3: Event RMA regression slopes ± S.E. for Hg^{II} vs. Hg^0, Pearson correlation coefficients for Hg^{II} vs. Hg^0, RH, O_3, and PM_1 σ_{sp}, and ratios of $Hg^{II}:Hg^0$ and $Hg^{II}:THg$. *p < 0.05, **p < 0.001.

Event	m ± S.E.	Pearson's R-value				Hg ratio	
	Hg^{II}/Hg^0	Hg^{II} vs Hg^0	Hg^{II} vs RH	Hg^{II} vs O_3	Hg^{II} vs PM_1 σ_{sp}	$Hg^{II}:THg$ (%)	$Hg^{II}:Hg^0$ (unitless)
1	-0.52 ± 0.03	-0.63**	-0.37**	0.03	-0.55**	11 ± 3	0.12 ± 0.04
2	-0.45 ± 0.02	-0.55**	-0.28*	0.10	-0.11	9 ± 2	0.10 ± 0.03
3	-0.76 ± 0.01	-0.95**	-0.53**	0.71**	0.59**	9 ± 4	0.10 ± 0.04
4	-0.35 ± 0.02	-0.92**	-0.79**	NA	-0.40**	15 ± 5	0.18 ± 0.07
5	-0.52 ± 0.01	-0.96**	-0.50**	-0.74**	-0.71**	14 ± 4	0.16 ± 0.06
6	-0.41 ± 0.02	-0.75**	-0.60**	0.20*	0.40**	12 ± 3	0.13 ± 0.04
7	-0.37 ± 0.02	-0.75**	-0.78**	0.59**	0.20*	13 ± 2	0.16 ± 0.03
8	-0.21 ± 0.01	-0.74**	-0.58**	0.55**	-0.09	12 ± 2	0.13 ± 0.03
9	-0.46 ± 0.03	-0.76**	-0.63**	0.04	-0.46**	11 ± 4	0.13 ± 0.05
10	-0.40 ± 0.03	-0.16	-0.52**	0.20	-0.66**	10 ± 3	0.11 ± 0.03
11	-0.28 ± 0.01	-0.94**	-0.41*	-0.28	-0.76**	9 ± 2	0.09 ± 0.03
12	-0.29 ± 0.02	-0.41**	-0.61**	0.17	0.18	10 ± 2	0.11 ± 0.02
13	-0.45 ± 0.02	-0.85**	-0.71**	0.69**	0.49*	10 ± 4	0.11 ± 0.05
14	-0.18 ± 0.01	-0.53**	-0.11	0.07	-0.36*	10 ± 1	0.11 ± 0.02
15	-0.45 ± 0.02	-0.57**	-0.63**	0.87**	0.45*	9 ± 2	0.10 ± 0.02
16	-0.16 ± 0.01	-0.59**	-0.55**	0.13	-0.04	9 ± 1	0.10 ± 0.02
17	-0.46 ± 0.02	-0.74**	-0.78**	NA	0.64**	9 ± 2	0.09 ± 0.03
18	-0.45 ± 0.01	-0.82**	-0.81**	0.65**	0.76**	9 ± 2	0.09 ± 0.02

 By contrast, measurements of enhanced nighttime RGM at MBO during summer 2005 showed a slope nearer to unity for RGM versus GEM (-0.89) (Swartzendruber et al., 2006). These events, as well as other instances of enhanced RGM at MBO, were hypothesized to have UT/LS influence (Swartzendruber et al., 2006; Timonen et al., 2013). An aircraft study also reported an Hg^{II} versus Hg^0 regression slope for air originating from the upper troposphere that was similarly close to unity (-0.93), and a slope of -0.53 for stratospheric air (Lyman and Jaffe,

2012). The lack of mass closure under stratospheric influence was attributed to the idea that THg decreases toward the stratosphere while the ratio of Hg^{II}:Hg^0 simultaneously increases with altitude (Swartzendruber et al., 2006; Lyman and Jaffe, 2012). While a few slopes of individual events in the present study showed values closer to unity (e.g. Event 3 = -0.76 ± 0.01), the total slope of all events was much lower than that seen in air masses influenced by the UT/LS. Meanwhile, Fu et al. (2021) found a slope of -0.44 ± 0.10 for Hg^{II} versus Hg^0 during one event of free tropospheric air mass intrusion at PDM, similar to the mean slope we report here. Unlike the majority of events we identified at SPL, they reported a lack of common air mass origins across their eight-day event and after correcting for this based on reported latitudinal GEM differences, they obtained a corrected slope of -0.88 implying that most of the Hg^{II} was retained within the sampled air masses. Given the relative consistencies in air mass origins (Figure A3) during our events, the majority of which were 5 days or fewer (Table 2), we did not attempt such a correction.

Instead, we propose that the lack of mass closure may be caused by upwind Hg^0 oxidation followed by Hg^{II} loss via deposition during transport, or scavenging of Hg^{II} by cloud droplets (Fu et al., 2021; Lyman and Jaffe, 2012; Swartzendruber et al., 2006), explanations which are further supported by the modeled transport behavior during events at SPL. During all high Hg^{II} events at SPL in 2021 and 2022, the air mass back trajectories generally maintained transport within the low to mid-free troposphere over the Pacific Ocean before subsiding over the continent (Fig. A3). The back trajectories from all 18 events spent an average of 12 ± 2% and a maximum of 16% of total transport time in the PBL. Moreover, HYSPLIT-STILT transport analysis showed that event air masses spent on average just 13 ± 5% (Fig. 4), and a maximum 24% of transport time above 6 km AGL. The median percent transport time spent in the 3 to 5 km range (chosen here to approximate the low-mid free troposphere) during the events was 43%. The nine air masses that spent greater than 43% of their transport at these altitudes had significantly (p < 0.001) higher mean Hg^{II} concentrations (142 ± 23 pg m^{-3}) and spent significantly less time in the 0 to 2 km range (30 ± 3%) than those that spent less than 43% of transport in this altitude range (114 ± 11 pg m^{-3}; 38 ± 4% of transport in 0 to 2 km altitude range). The relatively limited influence from both the UT/LS and PBL on the sampled air masses indicated that extended periods of elevated Hg^{II} at SPL likely originated in the low to mid-free troposphere (Fig. 4). A comparison to transport pathways of air masses associated with low Hg^{II} is described in Sect. 3.2.3.
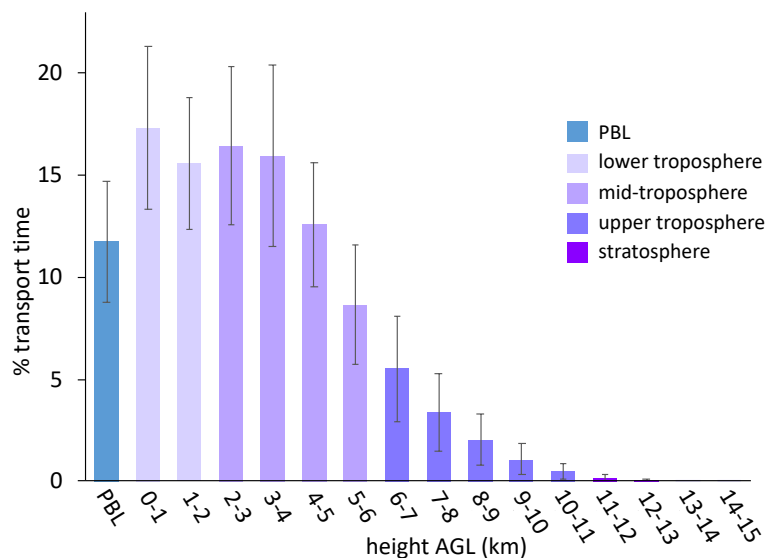
520

Figure 4: The percentage of transport time that high Hg^{II} event air masses spent at each altitude above ground level (AGL) averaged across all 18 events. In general, the majority of air mass transport fell in the low to mid altitudes, while the air masses spent less of the transport time within the planetary boundary layer (PBL) or in the upper troposphere / lower stratosphere (UT/LS). Bars are color-coded by layers of the

525 **atmosphere. The PBL was explicitly calculated by the HYSPLIT-STILT model, but the other altitude groupings are general approximations.**

All HYSPLIT-STILT runs demonstrated that SPL experienced prevailing westerlies during the 18 events, as has been demonstrated in earlier work at the site (Faïn et al., 2009; Hallar et al., 2016). However, there was not a consistent directional origin evident by season (Fig. A3), or in relation to covariance in other air mass tracers (Sect.

530 3.2.2) during high Hg^{II} events. There was also large variability in whether the event air masses originated over the central Pacific, north Pacific, or southwest as well as the horizontal distance covered in 10 days of transport. Although 10 events showed some or all back trajectories approaching SPL from the southwest, there did not appear to be any consistency in air mass speed, altitude, or composition amongst this subgroup. The horizontal transport pathway alone, therefore, did not appear to directly influence the presence of high concentrations of Hg^{II} at SPL.

535 There was some variation in the amount of time the simulated air masses spent over the North American continent (50 to 150 hours of the 10-day transport), but differences were not associated with particular air mass compositions. Simulated air mass temperature was most dependent on season, but generally increased over the continent. Additionally, all event back-trajectories showed some upwind precipitation during the 10 days, but no precipitation within at least 50 hours of arrival at SPL. Simulated cloud cover during transport was generally higher

540 (60–80%) upwind of SPL, and dropped substantially prior to the end of the trajectories, in most cases reaching near 0% by arrival at SPL. These indices could account for the lack of mass closure between Hg^{0} and Hg^{II}. Relative humidity remained below 60% during transport, and consistently declined as the air masses approached the site. Therefore, the air masses in which high Hg^{II} was measured at the site were generally dry, and did not experience significant washout close to the measurement site.

545   In another study at MBO, maximum RGM:GEM ratios ranged from 0.16 to 1.05 during high RGM periods, with the largest ratios seen in air masses influenced by the marine boundary layer (MBL) that were marked by circulation above the ocean for at least 10 days prior to arrival at MBO as well as decreases in CO, aerosol scattering, and O_3 (Timonen et al., 2013). Timonen et al. (2013) defined MBL events as clean air masses that circled above the ocean for at least 10 days prior to arrival at MBO, where enhancements in RGM coincided with decreases

550   in CO, aerosol scattering, and O_3, as well as no indication of UT/LS influence. These MBL events were associated with higher concentrations of RGM and larger RGM/GEM ratios than seen at SPL (Table 3). By comparison, the mean ratio (s.d.) of Hg^{II}:Hg^0 during the 18 events at SPL was 0.12 ± 0.03, and maximum values ranged from 0.13 to 0.29 (a comparison of these values to non-event times will be discussed in Sect. 3.2.3). Mean ratios during the summer 2021 Events 4–8 (0.15 ± 0.02) were significantly higher than the rest of the events in the study (0.10 ± 0.01)

555   ($p < 0.001$), possibly related to mean Hg^{II} concentrations being significantly higher in summer 2021 than in other seasons (Sect. 3.1.1). Nevertheless, air masses at SPL did not show behavior or composition comparable to that of MBL-influenced air at MBO. Understandably, by nature of the site locations, the air masses measured at SPL spent much more time over the continent (Fig. A3), potentially allowing for more scavenging of Hg^{II} during transport, and therefore resulting in Hg^{II} vs. Hg^0 regression slopes further from unity and a lower ratio of Hg^{II}:Hg^0.

560   In conclusion, based upon the results of the HYSPLIT-STILT and other meteorological analysis, we posit that the lack of mass closure in the slopes of Hg^{II} versus Hg^0 regressions during the 18 events at SPL was likely caused by distant upwind oxidation followed by Hg^{II} loss via deposition or cloud droplet uptake during transport. This finding is further supported by the analyses of trace gas measurements and of select non-event periods below.

3.2.2 Event Air Mass Composition

565   Concentrations and relationships between other trace gases measured in this study varied across the events. Of the 16 events with sufficient O_3 measurement coverage, seven showed significant positive correlations between Hg^{II} and O_3 (Events 3, 6, 7, 8, 13, 15, and 18), and six of these seven events also had significant positive correlations between Hg^{II} and aerosol PM_1 scattering (all but Event 8) (Table 3). These events were mostly in summer, but occurred in both study years. Event 3 is shown in the Appendix as an example of this type of event (Fig. A4). Ozone

570   concentrations increased by approximately 10 to 20 ppbv during these events, concurrent with fluctuations in Hg^{II} concentrations. Meanwhile, the magnitudes of aerosol PM_1 scattering enhancements were more varied, ranging from approximately 30 to 120 Mm^{-1}; in part because scattering was generally lower during spring than summer, and some of the summer events also showed evidence of smoke (Sect. 2.3.1).

While Faïn et al. (2009) reported similar transport altitudes for air masses associated with enhanced Hg^{II} at

575   SPL, they reported no relationship between Hg^{II} and O_3. Previous studies at the MBO and PDM mountaintop sites, however, also showed co-enhancements of Hg^{II} and O_3. Often, these enhancements occurred with simultaneous decreases in Hg^0, CO, and aerosol scattering, which Swartzendruber et al. (2006), Timonen et al. (2013), and Fu et al. (2016) attributed to Hg^{II} transport from the UT/LS. As previously discussed, however, HYSPLIT-STILT transport analysis during events at SPL did not show air masses at high enough altitudes to indicate UT/LS influence

580 in the 10 days of simulated transport (Fig. A3), and thus we suggest that UT/LS air was not the source of co-enhanced O_3 and Hg^{II} in these events.

High O_3 concentrations could also be generated as a secondary product of natural or anthropogenic combustion. For example, Timonen et al. (2013) reported events of enhanced Hg^{II}, O_3, aerosol scattering, and CO at MBO during springtime, when meteorological conditions favor long-range trans-Pacific air mass transport and can

585 deliver anthropogenic pollution from the Asian continent (Timonen et al., 2013). Maximum O_3 concentrations during the seven events at SPL ranged from 58 to 74 ppbv, values which were comparable to the maximum O_3 values reported at MBO during events of high Hg^{II} associated with influence from Asian long-range transport, which ranged from 69 to 77 ppbv (Timonen et al., 2013). However, all of the events in this study with positive correlations between Hg^{II} and O_3 occurred during summertime, with the exception of Event 3 during spring 2021 (Fig. A4). In

590 all cases except for Event 8, back trajectories did not show transport from the Asian continent in the 10-day histories (Fig. A3). Alternatively, O_3 could have been picked up from the North American PBL and mixed with free tropospheric air as the air masses traveled over the continent before arriving at SPL, or O_3 could have been produced in conjunction with Hg^{II}, as their chemical production mechanisms both involve photochemical processes in dry air conditions.

595 The enhancement of O_3 during some summer events could also be a result of biomass burning, as ozone can be a secondary product in smoke plumes of wildfires (Briggs et al., 2016). Eight of the 18 events occurred when SPL was in smoke from local or regional wildfires and experiencing elevated concentrations of combustion tracers, particularly CO and aerosol scattering (Sect. 2.3.1, Table 2). Both O_3 and CO were significantly positively correlated with Hg^{II} during three events (Events 13, 15, 18), and CO was above 150 ppbv during five events when

600 Hg^{II} was significantly correlated with O_3 (Events 6, 7, 8, 13, 18). Four events where Hg^{II} was correlated with O_3 also showed positive correlations between O_3 and CO (Events 6–8, 18). Biomass burning has been shown to volatilize stored Hg as Hg^0 and release it to the atmosphere. High levels of Hg^{II} have not typically been reported in smoke plumes (McLagan et al., 2021; Obrist et al., 2007; Friedli et al., 2003), though all published measurements were collected using denuder-based methods. Elevated Hg^{II} concentrations during the events under consideration here,

605 which had concentrations of Hg^0 comparable to the seasonal means, may be coincidental to the presence of smoke in the air masses; i.e., it is possible that the smoky air was mixed with cleaner free tropospheric air containing higher concentrations of Hg^{II}. However, it is also possible that co-emitted halogens or aerosols in smoke plumes led to faster oxidation or scavenging of Hg^0 than in clean air, leading to elevated Hg^{II} and PBM. Further work is needed to characterize the concentrations and chemistry of Hg^0 and Hg^{II} in smoke plumes using verified measurement

610 methods.

Seven of the 18 events showed significant anticorrelations between Hg^{II} and PM_1 scattering (Events 1, 4, 5, 9, 10, 11, 14; Table 3). Oxidized Hg in these events also tended to be significantly anticorrelated with NO_x, but not always with other pollution tracers. Three of these events occurred when SPL was in smoke, and therefore PM_1 scattering was elevated, but showed measurable decreases when Hg^{II} increased, indicating that SPL may have

615 experienced some influence from cleaner, free tropospheric air during these smoky periods. Event 5 (June 13 23:00 – June 15, 2021 21:00 MST) (Fig. A5) was the only one of these cases where Hg^{II} was significantly anticorrelated

with O_3 (Pearson's R = -0.74, p < 0.001), and was also anticorrelated with NO_x (Pearson's R = -0.43, p < 0.001) and SO_2 (Pearson's R = -0.34, p < 0.05). This event also had a particularly strong anticorrelation between Hg^{II} and Hg^0 (Pearson's R = -0.96, p < 0.001) and RH (Pearson's R = -0.50, p < 0.001), and notably higher-altitude transport than other events (Fig. A5); the air mass spent 23% of transport time higher than 6 km AGL, compared to an average of $13 \pm 5\%$ for all events. Considering these factors, Event 5 appeared to have particularly clean air conditions, originating from higher in the free troposphere. However, the altitudes associated with Event 5 air mass transport were still not high enough to be considered UT/LS influenced, as the air mass trajectories spent 93% of transport time below 8 km AGL.

The occurrence of events with either positive or negative relationships with aerosol scattering could be related to the relative abundance of gaseous versus particulate Hg^{II} (e.g. RGM/GOM vs. PBM). For example, an enhancement in aerosol scattering could indicate a higher proportion of PBM than during other events of elevated Hg^{II}, whereas events with lower aerosol scattering could indicate more gaseous Hg^{II}. A study at PDM showed that during events of elevated PBM, measured with the Tekran speciation system, aerosol number concentration was significantly anticorrelated with PBM (Fu et al., 2016). The authors posited that this relationship could indicate that atmospheric aerosol concentration may not play a significant role in PBM formation in the middle and upper free troposphere, or rather that aerosol number concentration at PDM is driven by anthropogenic influence from the PBL, and is therefore not representative of the composition of the middle to upper free troposphere at that site (Fu et al., 2016). However, it is difficult to directly and quantitatively compare aerosol number concentrations reported by Fu et al. (2016) with the aerosol scattering measurements made at SPL, given that scattering is also affected by aerosol size distribution. Moreover, because the dual-channel Hg measurement system does not differentiate between gaseous and particle phases of Hg^{II}, any relationship between these variables is speculative at this time.

3.2.3 June 2022 case study

June 2022 contained five distinct events of elevated Hg^{II} (Events 11–15), with periods of low Hg^{II} in between events (referred to here as "non-events" and numbered 1 through 5) (Fig. 5). The five events during this period had characteristics similar to the other 13 events from this study, such as depleted Hg^0 and low RH, but displayed variation in transport pathways, meteorology, and trace gas concentrations. More specifically, all the June 2022 events had strong and significant anticorrelations between Hg^{II} and Hg^0 (Pearson's R = -0.94 to -0.41, p < 0.001; Table 3), whereas the non-event Hg^{II} versus Hg^0 anticorrelations were either weaker (Non-Events 1, 3, and 5) or not significant at the p < 0.05 level (Non-Events 2 and 4) (Table A2).
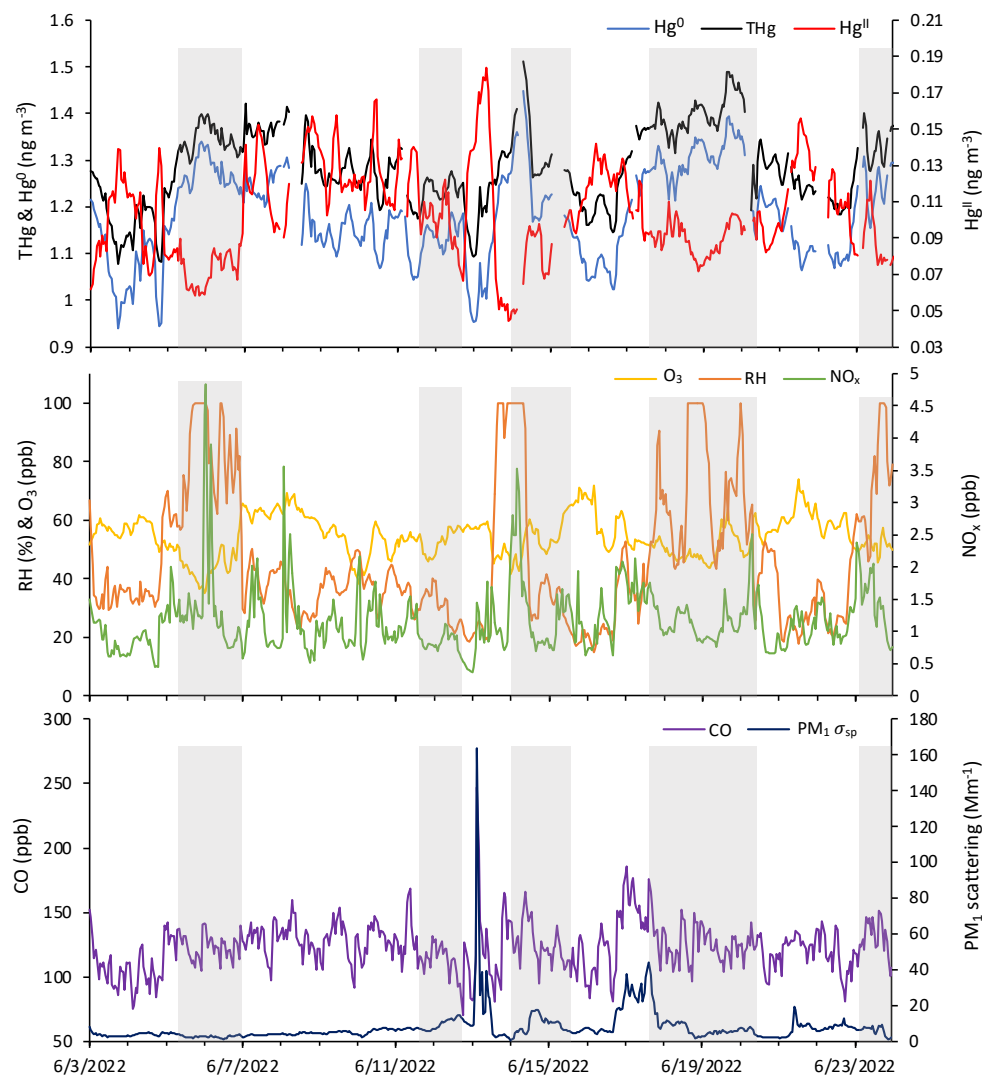
Figure 5: Time series of (a) Hg^{II}, Hg^0, THg, (b) RH, O$_3$, NO$_x$, and (c) CO, and aerosol PM$_1$ scattering for June 3 04:00–June 24, 2022 03:00 MST, showing the five events of enhanced Hg^{II} that occurred in June 2022, and the five corresponding non-events (shaded in gray).

650

The non-event air masses spent a significantly smaller percentage of transport time in the 3 to 5 km altitude range (26 ± 4%) than the event air masses (40 ± 7%) (p < 0.05) (Fig. A6). Generally, event air masses tended to spend more time at altitudes associated with the low to mid-free troposphere, whereas non-event air masses spent more time at lower altitudes and in the PBL (Fig. A6 and A7). June event air masses spent 52% of transport time

655 above 3 km, whereas non-events spent 44% of transport time above 3 km. Additionally, the high Hg^{II} events showed significantly higher mean Hg^{II} and O$_3$ concentrations, and significantly lower mean Hg^0, RH, and NO$_x$ concentrations than the non-events (Table 4). The ratio of Hg^{II}:Hg^0 was also significantly higher (p < 0.05) during events (10 ± 1%) than non-events (6 ± 1%), and the amount of THg measured as Hg^{II} was also significantly (p < 0.001) higher during events (10 ± 1%) than non-events (7 ± 1%). Simulated precipitation for the air masses prior to

660   arrival at SPL showed precipitation up to the simulation end time in Non-Events 3, 4, and 5. The higher RH during non-event times concurrent with lower Hg^{II} concentrations could indicate greater wet deposition or scavenging by clouds of Hg^{II} than during event periods. Events 13 and 14 occurred when SPL was influenced by smoke from regional wildfires in Arizona and New Mexico, so both CO and aerosol scattering were elevated (Table 2). Figure 6 shows example transport models for Event 11 (June 3 04:00 – June 5, 2022 04:00 MST) and Non-Event 1 (June 5

665   05:00 – June 6, 2022 23:00 MST). Event 11 showed higher transport altitudes, lower RH, and no precipitation directly prior to arrival at SPL, whereas Non-Event 1 had lower atmospheric transport, higher RH, and more recent precipitation. The differences between events and non-event periods demonstrated that the commonalities in event air mass composition and transport could be attributed to the specific conditions under which Hg oxidation occurred in the upwind atmosphere, as opposed to ambient atmospheric conditions seen locally at SPL.

670

Table 4: June 2022 event vs non-event mean ± s.d. for Hg species, THg, RH, PM$_1$ σ$_{sp}$, and trace gases. Bolded values are significantly different at the p < 0.05 level.

	Hg^{II} $(pg\ m^{-3})$	Hg^{0} $(ng\ m^{3})$	THg $(ng\ m^{3})$	RH $(\%)$	NO_x (ppb)	O_3 (ppb)	CO (ppb)	PM$_1$ σ_{sp} (Mm^{-1})
Events	**112 ± 23**	**1.1 ± 0.1**	1.3 ± 0.1	**37 ± 15**	**1.1 ± 0.4**	**57 ± 6**	120 ± 20	6.7 ± 5.4
Non-Events	**85 ± 16**	**1.3 ± 0.1**	1.4 ± 0.1	**65 ± 26**	**1.3 ± 0.6**	**49 ± 6**	130 ± 20	7.8 ± 7.1

675
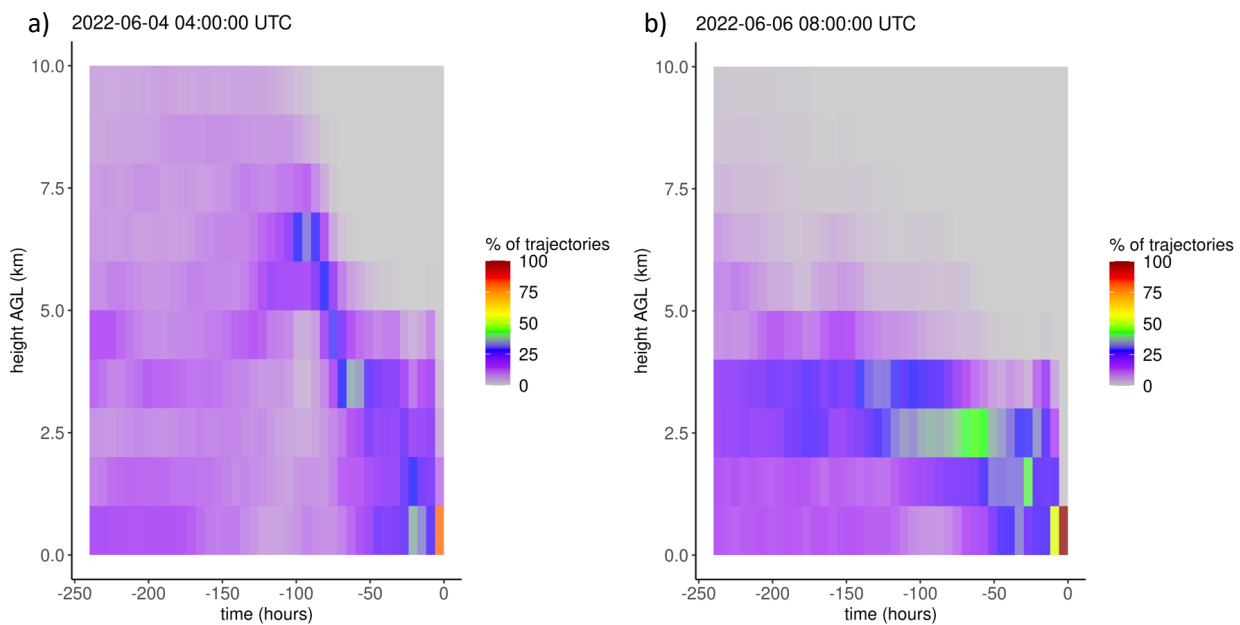
Figure 6: Example vertical distributions of air mass trajectories for (a) Event 11 and (b) Non-Event 1. Shading reflects the percentage of backward trajectories within a given altitude bin when aggregated to 6-hour intervals.

3.3 Principal Components Factor Analysis (PCA)

Broadening these event-based analyses to the rest of the hourly measurement data, three factors explaining 60–70% of the total variance were generated in the PCA data reduction technique applied to each of the sampled seasons in 2021 and 2022 (Table B1 and B2), and for the combined 2022 spring–summer period (Table 5). Although differences appeared in the magnitude and sign of variable loadings for each period, there were some notable features that all simulations had in common, as well as some consistent seasonal patterns. For example, all solutions contained two common factors: one representing clean background air with evidence of Hg oxidation (little to no loading of most combustion tracers, and inverse loadings of Hg^0 and Hg^{II}), and another representing anthropogenic and/or biogenic combustion (with some combination of CO, NO_x, aerosol scattering, O_3 and Hg^0 loading having the same sign). In summer 2021 this factor explained the largest percent variance (32%) and was likely dominated by the aforementioned biomass burning signature, whereas in summer 2022 it explained just 23% of the variance and likely represented other local regional combustion sources (Tables B1-B2). The third factor varied in its makeup, but in at least the 2022 applications there were shared loadings of pressure, water vapor mixing ratio and aerosol scattering, and an inverse loading of CO. Another consistent feature was that Hg^{II} almost exclusively loaded inversely with Hg^0, and on any factor where the two variables did display the same sign, one or both of their loadings were very small (< 0.3). Oxidized Hg was usually, but not always, inversely related to water vapor mixing ratio, and in some solutions was positively associated with O_3 and aerosol scattering but did not load strongly with factors representing combustion sources. These broader features are complimentary with the relationships observed during events of high Hg^{II} (Sect. 3.2).

Table 5: Factor loadings of each variable and the percentage of total variance explained by each factor, as obtained from Principal Components Analysis for the spring-summer 2022 period.

	2022 - All		
	Factor 1	Factor 2	Factor 3
pressure	0.89	0.17	-0.08
wvmr	0.86	-0.22	0.04
Hg^0	0.12	-0.66	0.51
Hg^{II}	0.11	0.78	-0.20
CO	-0.42	-0.04	0.76
O_3	-0.02	0.72	0.17
NOx	0.25	0.00	0.77
PM_1 σ_{sp}	0.59	0.53	0.26
Variance Explained	30%	24%	17%

Here we describe the results of PCA application to the combined period of 1 March – 15 September, 2022 (Table 5); summaries of the individual spring and summer seasons are provided in the Appendix. Factor 1 (30%) had strong positive loadings of pressure, water vapor, and aerosol scattering with a moderate negative loading of CO. This factor may represent particle climatology given SPL's history of spending a significant fraction of time in-cloud and evidence for new particle formation during particular seasons and times of day (Hallar et al., 2016). Factor 2 (24% of variance) reflects observations of Hg oxidation within the clean, dry, remote free troposphere. Interestingly, both ozone and aerosol scattering loaded strongly with the same sign as Hg^{II} on this factor, a feature that also appeared to some degree in spring 2021 and in the separate analyses of spring 2022 and summer 2022. As shown in Sect. 3.2.2, about one third of the 18 high Hg^{II} events also had positive correlations for Hg^{II} versus O_3 and Hg^{II} versus aerosol scattering. These relationships may point to the potential for Hg oxidation in the presence of ozone, but not necessarily in air originating from the UT/LS. This may also suggest the propensity for Hg^{II} to be found in the particulate form at SPL in certain instances, but we cannot confirm this due to the current inability of the dual-channel system to distinguish between phases of Hg^{II} (e.g. GOM or PBM). Lastly, Factor 3 in 2022 (17% of variance) represents combustion sources with positive loadings of CO, NO_x, and Hg^0 with more moderate loadings of O_3 and aerosol scattering. It is notable that in the full 2022 analysis, aerosol scattering distributed almost uniformly across all three factors, suggesting multiple drivers for the presence of aerosols at the site that likely vary by season, as evident in the separate spring and summer analyses.

4. Conclusions

In this study, we examined air mass composition and transport of events of elevated Hg^{II} at SPL, a high elevation mountaintop site, over two six-month periods in spring and summer 2021 and 2022. Unlike previous studies at mountaintop sites, we employed a dual-channel Hg measurement system, which was calibrated with an SI-traceable calibration system and shown to produce unbiased measurements of Hg^{II} (Elgiar et al., 2024). Elemental

Hg concentrations and patterns at SPL were similar to those reported in previous work, but mean and maximum Hg^{II} concentrations in this study were approximately three times higher than earlier measurements at this site, and Hg^{II} comprised on average more than 10% of total atmospheric Hg during high Hg^{II} events. We also demonstrated that Hg concentrations at SPL were not affected by emissions from the three upwind coal-fired power plants, which can likely be attributed to power plant emission controls and lower Hg content in western U.S. coal. Events of elevated Hg^{II} showed evidence of upwind Hg^0 oxidation, followed by Hg^{II} loss during transport in the low to mid-free troposphere, and no evidence of UT/LS influence. PCA confirmed that Hg^{II} measured at SPL was a result of Hg oxidation in the background atmosphere.

Results from this study contribute to the current understanding of Hg oxidation in a remote continental atmosphere. Additionally, the implementation of the dual-channel system provided Hg measurements that were larger in magnitude and more accurate than commercially available instrumentation. Concurrent work related to this project at SPL further elaborates on the methodological improvements for measuring ambient Hg^0 and Hg^{II} (Elgiar et al., 2024), and the potential contribution of iodine as an emerging Hg oxidant (Lee et al., in review). Collectively, the results of this campaign will importantly advance the current understanding of ambient Hg origins, cycling, bioavailability, and ultimately ecosystem fate.

Appendices

765   *Appendix A. Events of High Oxidized Mercury*
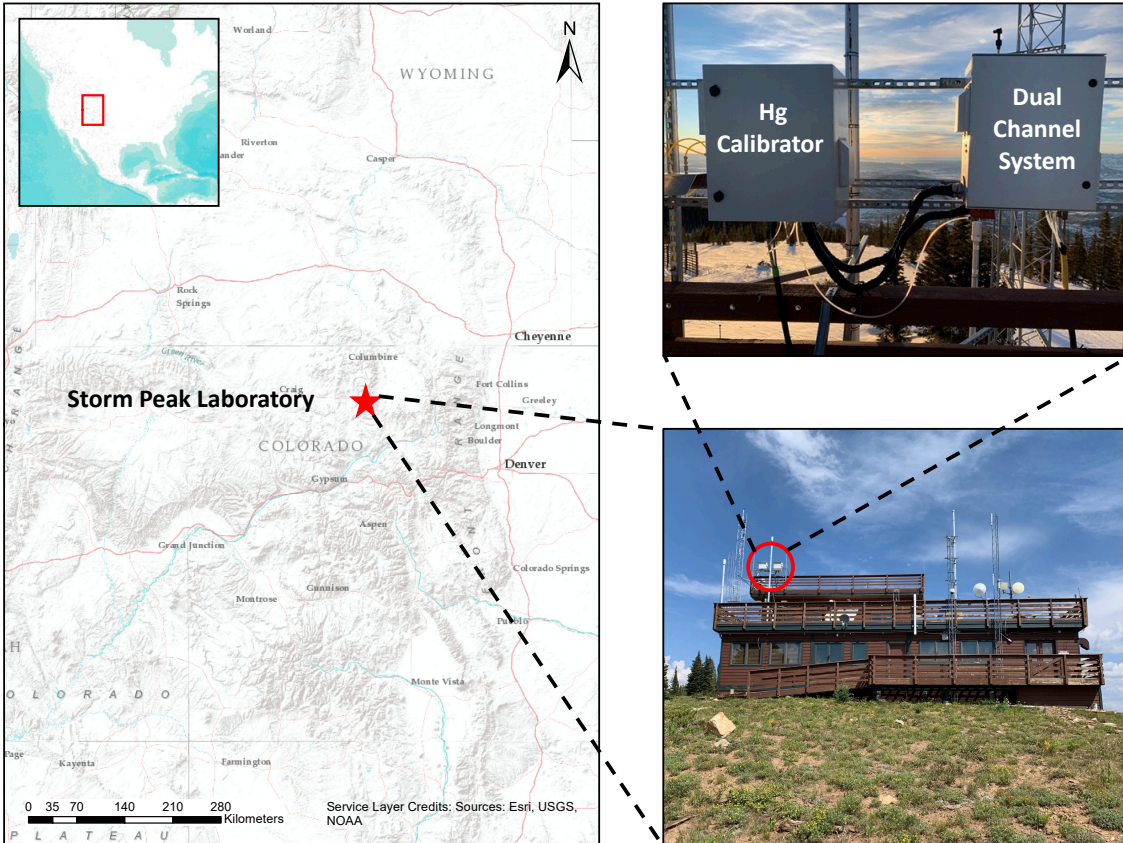
Figure A1: Site map of Storm Peak Laboratory and the location of the dual-channel system on the roof of the laboratory (Elgiar et al., 2024).
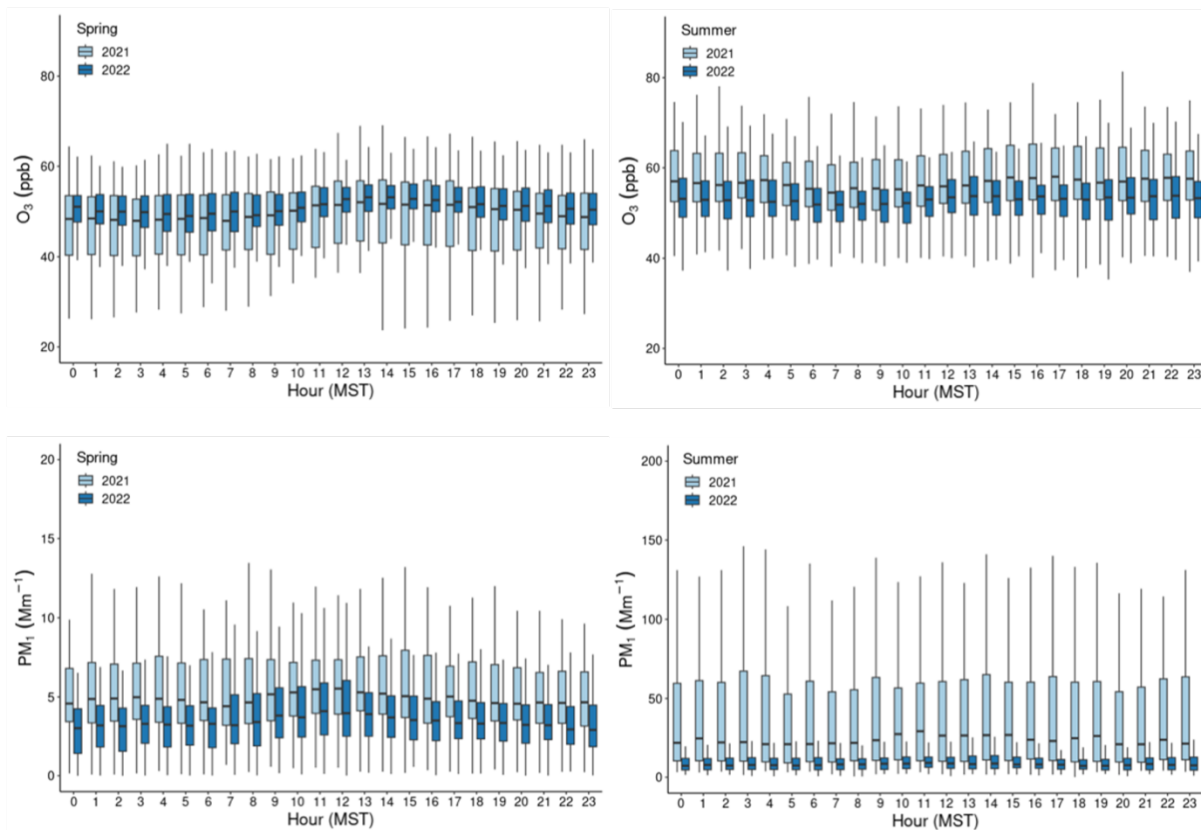
770 **Figure A2: Boxplots by hour of day (MST) for O_3 (top) and PM_1 σ_{sp} (bottom), showing diel variability during the spring (left) and summer (right) seasons of the study years. The centerline of each boxplot represents the median concentration, the box represents the interquartile range, and upper/lower whiskers are either the maximum/minimum value or the upper/lower quartile value plus/minus 1.5 times the interquartile range. Outliers are not shown.**

775
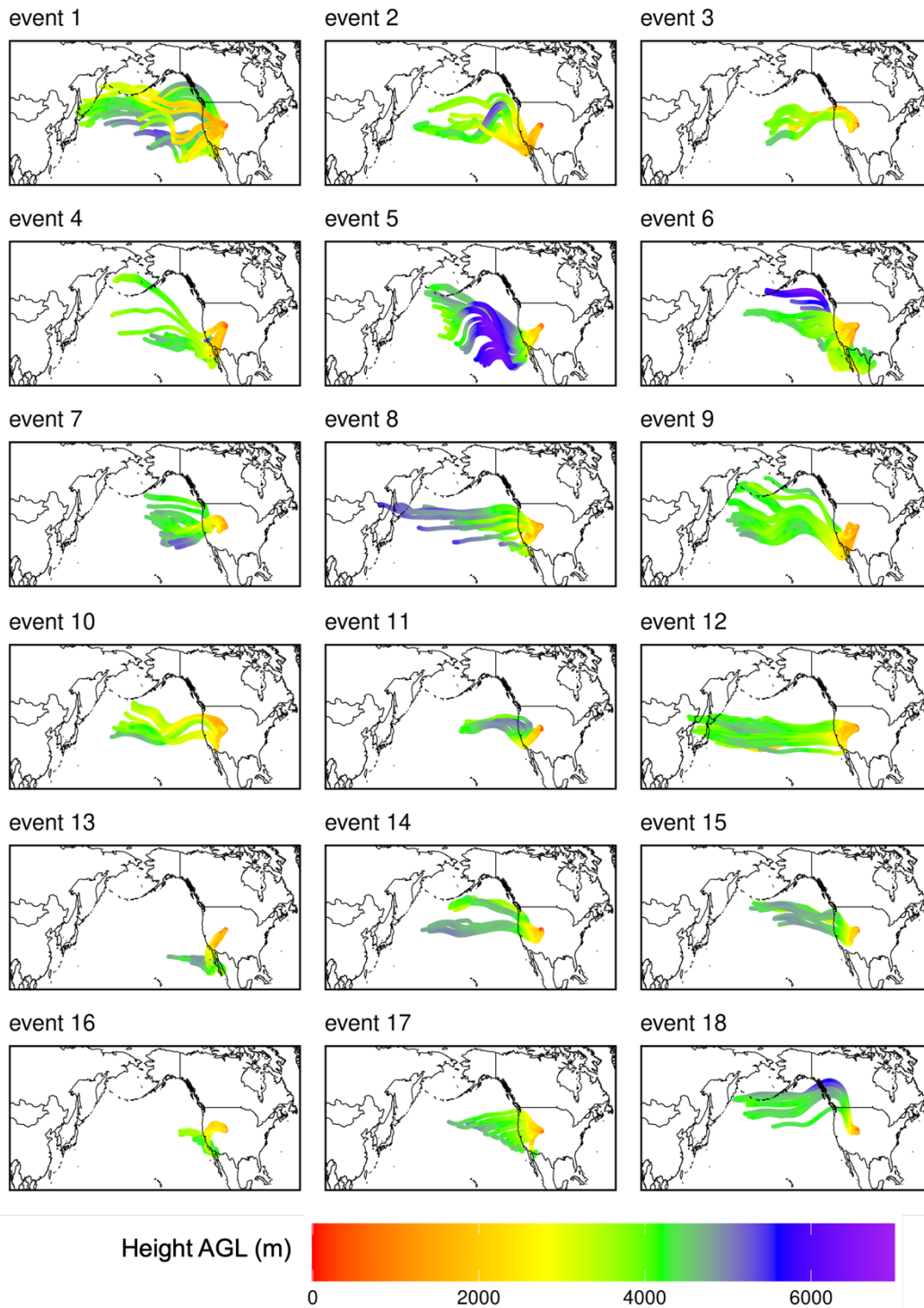
Figure A3: Composite maps of averaged HYSPLIT-STILT 10-day back trajectories for all 18 events of elevated Hg^{II}, color-coded by altitude AGL. Depicted trajectories represent the simulation average transport pathway of 1,000 backward trajectories, with simulations initialized at 3-hour intervals throughout each event.
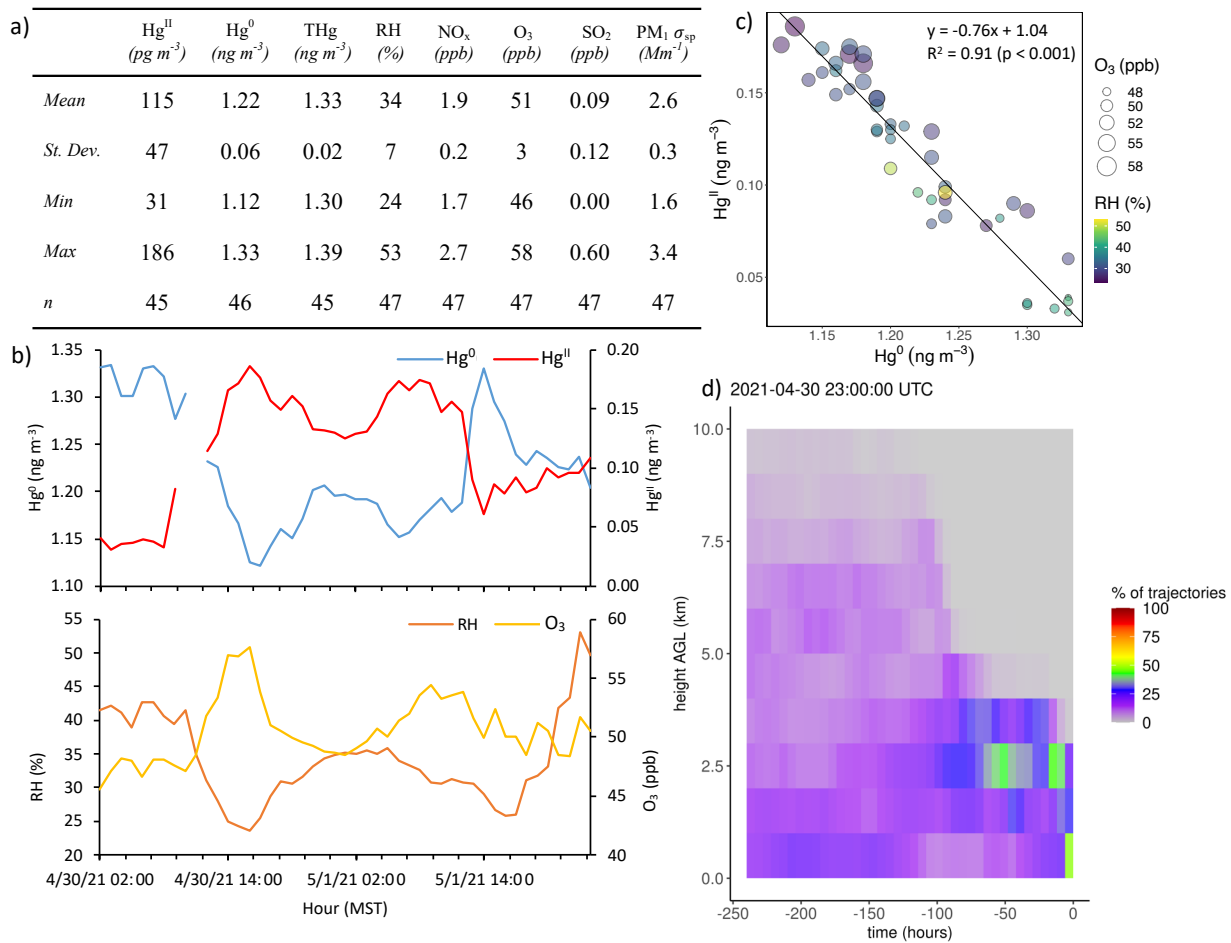
Figure A4: Event 3 (a) descriptive statistics, (b) time series of Hg^0, Hg^{II}, RH, and O$_3$, (c) scatterplot of Hg^{II} vs Hg^0 with RH and O$_3$, and (d) an example vertical profile of HYSPLIT-STILT backward trajectories, with the average mixed layer height represented by a black line.

785
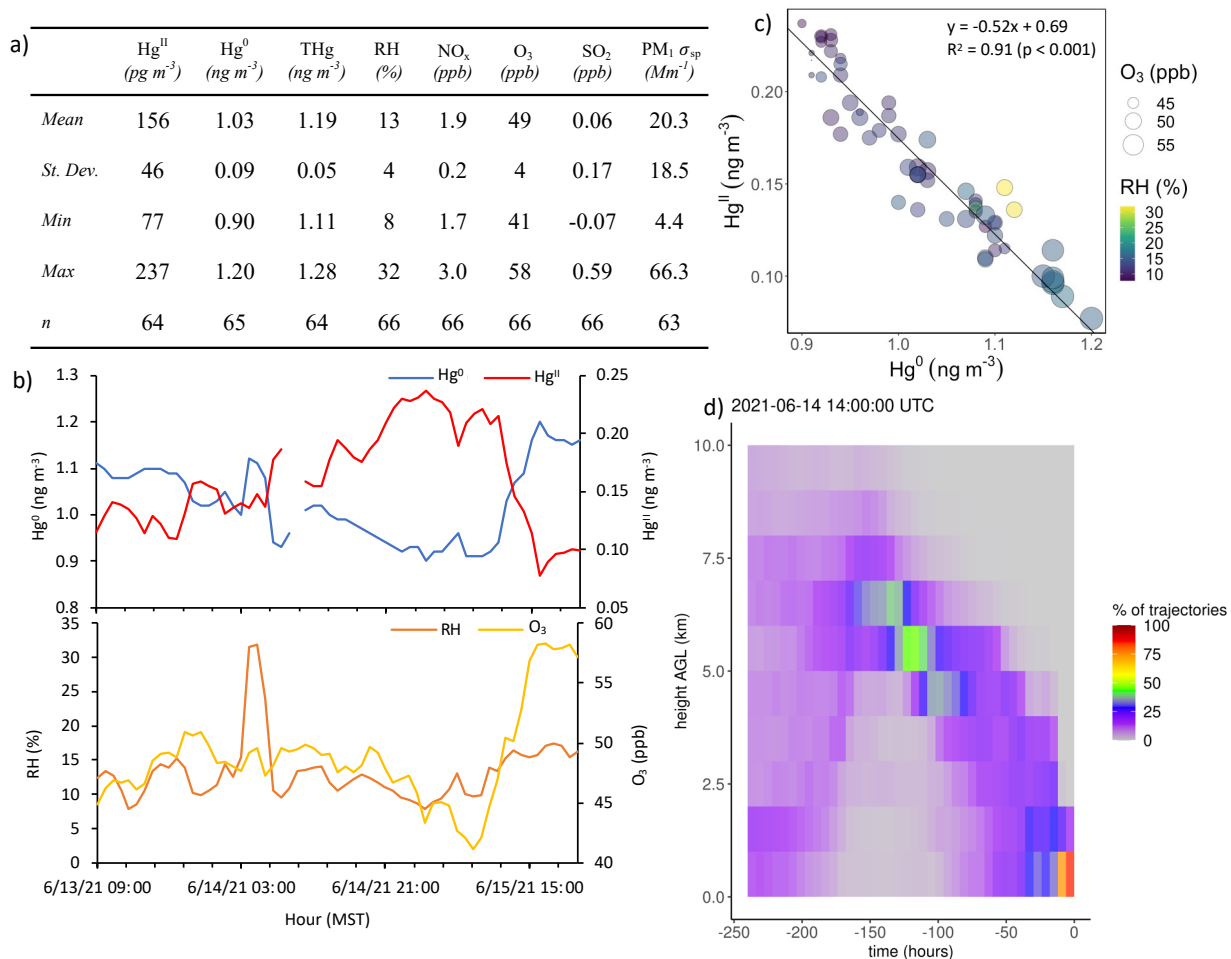
790

Figure A5: Event 5 (a) descriptive statistics, (b) time series of Hg⁰, Hgᴵᴵ, RH, and O₃, (c) scatterplot of Hgᴵᴵ vs Hg⁰ with RH and O₃, and (d) an example vertical profile of HYSPLIT-STILT backward trajectories, with the average mixed layer height represented by a black line.
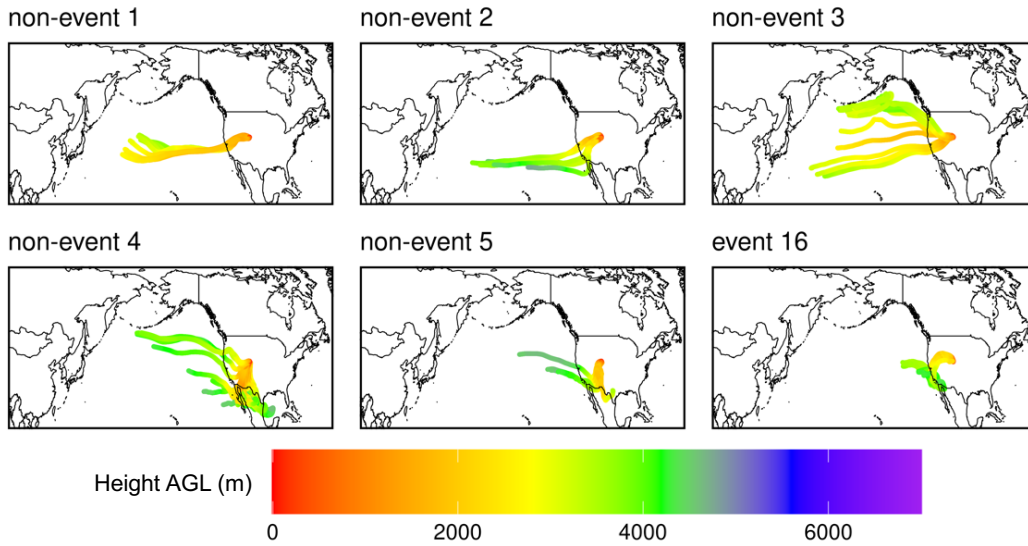
Figure A6: Composite maps of averaged HYSPLIT-STILT 10-day back trajectories for the five Non-Events in the June 2022 case study.
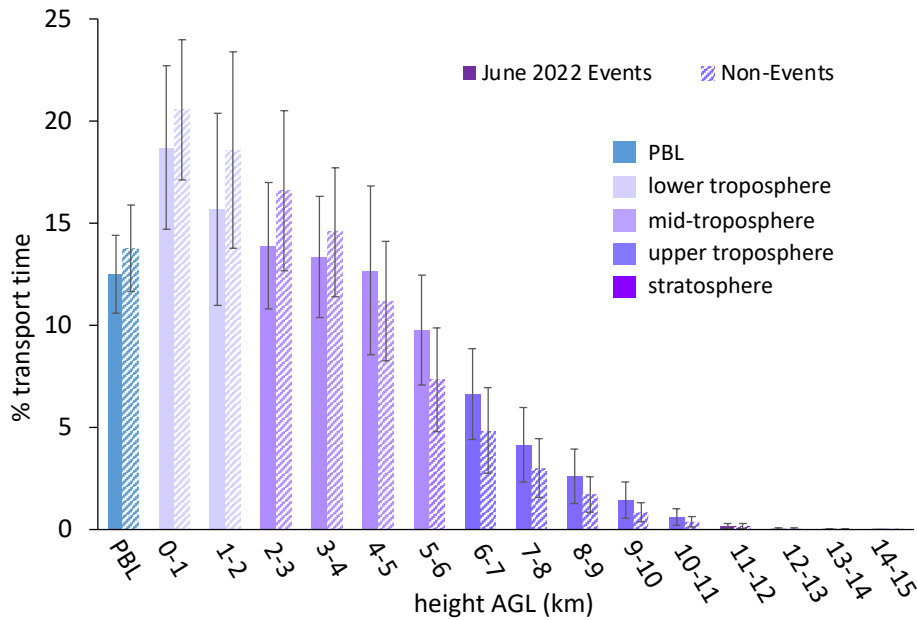
Figure A7: The percentage of transport time that high Hg^{II} event air masses spent at each altitude above ground level (AGL) averaged for the five June 2022 events and the corresponding June 2022 non-events. Event air masses tended to spend more time at altitudes associated with the low to mid-free troposphere, whereas non-event air masses spent more time at lower altitudes and in the PBL. Bars are color-coded by

layers of the atmosphere. The PBL was explicitly calculated by the HYSPLIT-STILT model, but the other
805   altitude groupings are general approximations.

Table A1: Pearson's correlation coefficients and p-values for Hg^{II} versus water vapor mixing ratio (wvmr) for all data in the study period, and for all times when relative humidity was below 85%, to limit the analysis to outside of periods when SPL was in cloud. While Hg^{II} and wvmr were generally significantly anticorrelated,
810   making it a strong variable for PCA, but RH had the most robust relationship with Hg^{II}, similar to previous studies at SPL (Faïn et al., 2009). Significance is defined as *$p < 0.05$, **$p < 0.001$.

Hg^{II} v.s. wvmr	All data	RH < 85%
Spring 2021	-0.12**	-0.04
Summer 2021	-0.54**	-0.54**
Spring 2022	0.05	0.17**
Summer 2022	-0.53**	-0.50**
All data	-0.12**	-0.24**

815   Table A2: Pearson correlation coefficients for the five Non-Events from the June 2022 case study. *$p < 0.05$, **$p < 0.001$.

Hg^{II} v.s.	Hg^0	RH	O_3	CO	$PM_1\ \sigma_{sp}$
Non-Event 1	-0.45*	-0.57**	0.51*	0.13	-0.07
Non-Event 2	-0.13	-0.32	0.13	-0.14	0.49*
Non-Event 3	-0.50*	-0.83**	0.87**	-0.34	0.56*
Non-Event 4	-0.13	-0.42**	0.46**	-0.19	0.24
Non-Event 5	-0.59*	-0.63*	0.25	0.46*	0.42

820   In both spring periods, Factor 1 (27–28% of total variance) was most notably marked by large inverse loadings of Hg^0 and Hg^{II}. In spring 2021, Factor 1 also had strong loadings of pressure and aerosol scattering of the same sign with Hg^{II}, whereas in spring 2022 there were strong loadings of CO and NO_x with the opposite sign to Hg^{II}. Notably, both Hg^0 and Hg^{II} distributed strongly on Factors 2 and/or 3 during the spring seasons, but always inversely with one another. For Hg^{II}, this may be related to the two different temporal patterns driving Hg^{II}

825   concentrations in the observations, with a strong diel cycle of high daytime Hg^{II} in the early spring (Sect. 3.1) along with the multi-day episodes of high Hg^{II} seen throughout the study period (Sect. 3.2). Meanwhile, Hg^0 also appeared to associate with the same sign as combustion tracers such as CO, NO_x, and/or O_3 as well as with water vapor mixing ratio (Table B1).

    The two summer periods showed more consistency between one another in terms of the distributions of

830   variables across different factors. In summer 2021, Factor 1 (32% of total variance) appeared to represent combustion with strong loadings of the same sign for CO, O_3, NO_x, and aerosol scattering and a weaker loading of Hg^0. A similar factor appeared in summer 2022, but as Factor 2 (23% of total variance) and with a weaker loading of ozone compared to 2021. The previously mentioned strong influence of local or regional wildfire smoke during at least one third of the summer 2021 period is likely driving the composition of Factor 1 in summer 2021, while the

835   reduced presence of underlying smoke in summer 2022 but still the existence of other regional combustion sources likely explains the presence of the combustion fingerprint as Factor 2 in summer 2022. Meanwhile, Factor 2 in 2021 (27% of variance) and Factor 1 in 2022 (33% of variance) are consistent with the proposed Hg oxidation in the background dry free troposphere, as indicated by a strong inverse loading of Hg^{II} with Hg^0 and also a strong inverse loading of Hg^{II} with water vapor mixing ratio, as well as very weak or inverse loadings of combustion tracers such

840   as CO or NO_x. Interestingly, in summer 2022 this factor also had a strong loading of ozone and a weak loading of aerosol scattering both with the same sign as Hg^{II}, but this was much less evident in summer 2021 (Table B2).

Table B1: Factor loadings of each variable and the percentage of total variance explained by each factor, as obtained from Principal Components Analysis for the spring seasons of 2021 and 2022.

	2021			2022		
	Factor 1	Factor 2	Factor 3	Factor 1	Factor 2	Factor 3
pressure	0.43	-0.22	-0.12	-0.09	0.30	0.66
wvmr	-0.18	-0.11	0.81	0.09	-0.22	0.76
Hg^0	-0.39	0.27	0.70	0.75	-0.35	0.15
Hg^{II}	0.73	-0.11	-0.14	-0.45	0.52	0.37
CO	--	--	--	0.72	0.08	-0.36
O_3	0.22	-0.76	0.27	0.04	0.69	-0.19
NOx	0.09	0.84	0.27	0.72	0.16	0.11
$PM_1 \, \sigma_{sp}$	0.80	0.17	0.02	0.02	0.80	0.17
Variance Explained	28%	18%	15%	27%	18%	16%

845

Table B2: Factor loadings of each variable and the percentage of total variance explained by each factor, as obtained from Principal Components Analysis for the summer seasons of 2021 and 2022.

	2021			2022		
	Factor 1	Factor 2	Factor 3	Factor 1	Factor 2	Factor 3
pressure	-0.09	0.06	0.92	0.06	0.05	0.94
wvmr	-0.21	0.85	0.01	0.82	0.24	0.20
Hg^0	0.28	0.84	0.06	0.78	0.31	0.03
Hg^{II}	0.11	-0.81	0.09	-0.83	0.06	0.01
CO	0.89	-0.15	-0.19	0.11	0.79	-0.39
O_3	0.51	-0.16	0.62	-0.67	0.23	0.18
NOx	0.67	0.29	0.11	0.19	0.79	0.14
PM_1 σ_{sp}	0.87	-0.15	0.17	-0.25	0.66	0.36
Variance Explained	32%	27%	16%	33%	23%	15%

Data availability

850   Ambient air data collected during this project is publicly available (Gratz et al., 2024).

Author contribution

LG, SL, AGH, and RV planned the campaign; TE, SL, LG, AGH, and NSH collected the measurements; SL and TE developed and improved the dual-channel Hg measurement system; ED, LG, TE, and NWH analyzed the data; JCL developed and TYW ran the HYSPLIT-STILT model; ED and LG wrote the manuscript; SL, AGH, RV, TYW,
855   CFL, PWP, NWH, JCL, TE, and NSH reviewed and edited the manuscript.

Competing Interests

The authors declare that they have no conflict of interest.

Acknowledgements

Funding for this work was provided by the National Science Foundation (NSF) Awards 1951513, 1951514,
860   1951515, 1951632. The authors thank Dr. Ian McCubbin, Dan Gilchrist, and Dr. Maria Garcia for assisting with instrument maintenance and data acquisition, Dr. Betsy Andrews of NOAA ESRL/GML for providing aerosol data, and Megan Ostlie for working up the trace gas data. Colorado College undergraduate students Brandon Chan and Zoe Zwecker contributed to the preliminary data analyses related to the results presented in this manuscript.

References

865   Andrews, E., Sheridan, P. J., Ogren, J. A., Hageman, D., Jefferson, A., Wendell, J., Alástuey, A., Alados-Arboledas, L., Bergin, M., Ealo, M., Hallar, A. G., Hoffer, A., Kalapov, I., Keywood, M., Kim, J., Kim, S.-W., Kolonjari, F., Labuschagne, C., Lin, N.-H., Macdonald, A., Mayol-Bracero, O. L., McCubbin, I. B., Pandolfi, M., Reisen, F., Sharma, S., Sherman, J. P., Sorribas, M., and Sun, J.: Overview of the NOAA/ESRL Federated Aerosol Network, Bulletin of the American Meteorological Society, 100, 123–135, https://doi.org/10.1175/BAMS-D-17-0175.1, 2019.

870   Ayers, G. P.: Comment on regression analysis of air quality data, Atmospheric Environment, 35, 2423–2425, https://doi.org/10.1016/S1352-2310(00)00527-6, 2001.

Benson, S. A.: How does Western coal affect mercury emissions?, EM: Air and Waste Management Association's Magazine for Environmental Managers, 32–34, 2003.

Bien, T. and Helmig, D.: Changes in summertime ozone in Colorado during 2000–2015, Elementa: Science of the
875   Anthropocene, 6, 55, https://doi.org/10.1525/elementa.300, 2018.

Bishop, K., Shanley, J. B., Riscassi, A., de Wit, H. A., Eklöf, K., Meng, B., Mitchell, C., Osterwalder, S., Schuster, P. F., Webster, J., and Zhu, W.: Recent advances in understanding and measurement of mercury in the environment: Terrestrial Hg cycling, Science of The Total Environment, 721, 137–647, https://doi.org/10.1016/j.scitotenv.2020.137647, 2020.

880   Briggs, N. L., Jaffe, D. A., Gao, H., Hee, J. R., Baylon, P. M., Zhang, Q., Zhou, S., Collier, S. C., Sampson, P. D., and Cary, R. A.: Particulate Matter, Ozone, and Nitrogen Species in Aged Wildfire Plumes Observed at the Mount Bachelor Observatory, Aerosol Air Qual. Res., 16, 3075–3087, https://doi.org/10.4209/aaqr.2016.03.0120, 2016.

Brodin, M., Helmig, D., and Oltmans, S.: Seasonal ozone behavior along an elevation gradient in the Colorado Front Range Mountains, Atmospheric Environment, 44, 5305–5315, https://doi.org/10.1016/j.atmosenv.2010.06.033,
885   2010.

Brown, R. J., Brown, A. S., Yardley, R. E., Corns, W. T., Stockwell, P. B.: A practical uncertainty budget for ambient mercury vapour measurement, Atmospheric Environment, 42, 2504–2517, https://doi.org/10.1016/j.atmosenv.2007.12.012, 2008.

Castro, P. J., Kellö, V., Cernušák, I., and Dibble, T. S.: Together, Not Separately, OH and O_3 Oxidize $Hg^{(0)}$ to $Hg^{(II)}$
890   in the Atmosphere, J. Phys. Chem. A, 126, 8266–8279, https://doi.org/10.1021/acs.jpca.2c04364, 2022.

Coburn, S., Dix, B., Edgerton, E., Holmes, C. D., Kinnison, D., Liang, Q., ter Schure, A., Wang, S., and Volkamer, R.: Mercury oxidation from bromine chemistry in the free troposphere over the southeastern US, Atmos. Chem. Phys., 16, 3743–3760, https://doi.org/10.5194/acp-16-3743-2016, 2016.

Collaud Coen, M., Andrews, E., Aliaga, D., Andrade, M., Angelov, H., Bukowiecki, N., Ealo, M., Fialho, P., Flentje, H., Hallar, A. G., Hooda, R., Kalapov, I., Krejci, R., Lin, N.-H., Marinoni, A., Ming, J., Nguyen, N. A., Pandolfi, M., Pont, V., Ries, L., Rodríguez, S., Schauer, G., Sellegri, K., Sharma, S., Sun, J., Tunved, P., Velasquez, P., and Ruffieux, D.: Identification of topographic features influencing aerosol observations at high altitude stations, Atmos. Chem. Phys., 18, 12289–12313, https://doi.org/10.5194/acp-18-12289-2018, 2018.

Custódio, D., Pfaffhuber, K. A., Spain, T. G., Pankratov, F. F., Strigunova, I., Molepo, K., Skov, H., Bieser, J., and Ebinghaus, R.: Odds and ends of atmospheric mercury in Europe and over the North Atlantic Ocean: temporal trends of 25 years of measurements, Atmos. Chem. Phys., 22, 3827–3840, https://doi.org/10.5194/acp-22-3827-2022, 2022.

Dibble, T. S., Tetu, H. L., Jiao, Y., Thackray, C. P., and Jacob, D. J.: Modeling the OH-Initiated Oxidation of Mercury in the Global Atmosphere without Violating Physical Laws, J. Phys. Chem. A, 124, 444–453, https://doi.org/10.1021/acs.jpca.9b10121, 2020.

Dowell, D. C., Alexander, C. R., James, E. P., Weygandt, S. S., Benjamin, S. G., Manikin, G. S., Blake, B. T., Brown, J. M., Olson, J. B., Hu, M., Smirnova, T. G., Ladwig, T., Kenyon, J. S., Ahmadov, R., Turner, D. D., Duda, J. D., and Alcott, T. I.: The High-Resolution Rapid Refresh (HRRR): An Hourly Updating Convection-Allowing Forecast Model. Part I: Motivation and System Description, Weather and Forecasting, 37, 1371–1395, https://doi.org/10.1175/WAF-D-21-0151.1, 2022.

Driscoll, C. T., Mason, R. P., Chan, H. M., Jacob, D. J., and Pirrone, N.: Mercury as a Global Pollutant: Sources, Pathways, and Effects, Environ. Sci. Technol., 47, 4967–4983, https://doi.org/10.1021/es305071v, 2013.

Dunham-Cheatham, S. M., Lyman, S., and Gustin, M. S.: Comparison and calibration of methods for ambient reactive mercury quantification, Science of The Total Environment, 856, 159–219, https://doi.org/10.1016/j.scitotenv.2022.159219, 2023.

Elgiar, T. R., Lyman, S. N., Andron, T. D., Gratz, L. E., Hallar, A. G., Horvat, M., Nair, S. V., O'Neil, T., Volkamer, R., and Živković, I.: Traceable Calibration of Atmospheric Oxidized Mercury Measurements, Environ. Sci. Technol., 58, 10706–10716, https://doi.org/10.1021/acs.est.4c02209, 2024.

Faïn, X., Obrist, D., Hallar, A. G., Mccubbin, I., and Rahn, T.: High levels of reactive gaseous mercury observed at a high elevation research laboratory in the Rocky Mountains, Atmos. Chem. Phys., 9, 8049–8060, https://doi.org/10.5194/acp-9-8049-2009, 2009.

Friedli, H. R., Radke, L. F., Lu, J. Y., Banic, C. M., Leaitch, W. R., and MacPherson, J. I.: Mercury emissions from burning of biomass from temperate North American forests: laboratory and airborne measurements, Atmospheric Environment, 37, 253–267, https://doi.org/10.1016/S1352-2310(02)00819-1, 2003.

925 Fu, X., Maruszczak, N., Heimbürger, L.-E., Sauvage, B., Gheusi, F., Prestbo, E. M., and Sonke, J. E.: Atmospheric mercury speciation dynamics at the high-altitude Pic du Midi Observatory, southern France, Atmos. Chem. Phys., 16, 5623–5639, https://doi.org/10.5194/acp-16-5623-2016, 2016.

Fu, X., Jiskra, M., Yang, X., Maruszczak, N., Enrico, M., Chmeleff, J., Heimbürger-Boavida, L.-E., Gheusi, F., and Sonke. J. E.: Mass-Independent Fractionation of Even and Odd Mercury Isotopes during Atmospheric Mercury
930 Redox Reactions, Environ. Sci. Technol., 55, 10164–10174, https://doi.org/10.1021/acs.est.1c02568, 2021.

Gkatzelis, G. I., Coggon, M. M., McDonald, B. C., Peischl, J., Gilman, J. B., Aikin, K. C., Robinson, M. A., Canonaco, F., Prevot, A. S. H., Trainer, M., and Warneke, C.: Observations Confirm that Volatile Chemical Products Are a Major Source of Petrochemical Emissions in U.S. Cities, Environ. Sci. Technol., 55, 4332–4343, https://doi.org/10.1021/acs.est.0c05471, 2021.

935 Gratz, L. E., Ambrose, J. L., Jaffe, D. A., Shah, V., Jaeglé, L., Stutz, J., Festa, J., Spolaor, M., Tsai, C., Selin, N. E., Song, S., Zhou, X., Weinheimer, A. J., Knapp, D. J., Montzka, D. D., Flocke, F. M., Campos, T. L., Apel, E., Hornbrook, R., Blake, N. J., Hall, S., Tyndall, G. S., Reeves, M., Stechman, D., and Stell, M.: Oxidation of mercury by bromine in the subtropical Pacific free troposphere, Geophysical Research Letters, 42, https://doi.org/10.1002/2015GL066645, 2015.

940 Gratz, L., Lyman, S., Elgiar, T., and Hallar, A. G.: Measurements of atmospheric mercury, trace gases, aerosols, and meteorology at Storm Peak Laboratory, Colorado, in 2021 and 2022, https://doi.org/10.5281/zenodo.10699270, 2024.

Gustin, M. S., Amos, H. M., Huang, J., Miller, M. B., and Heidecorn, K.: Measuring and modeling mercury in the atmosphere: a critical review, Atmos. Chem. Phys., 15, 5697–5713, https://doi.org/10.5194/acp-15-5697-2015,
945 2015.

Gustin, M. S., Dunham-Cheatham, S. M., Choma, N., Shoemaker, K. T., and Allen, N.: Determining sources of reactive mercury compounds in Reno, Nevada, United States, Front. Environ. Chem., 4, 1202957, https://doi.org/10.3389/fenvc.2023.1202957, 2023.

Gustin, M. S., Dunham-Cheatham, S. M., Lyman, S., Horvat, M., Gay, D. A., Gačnik, J., Gratz, L., Kempkes, G.,
950 Khalizov, A., Lin, C.-J., Lindberg, S., Lown, L., Martin, L., Mason, R., MacSween, K., Nair, S., Nguyen, L. S. P., O'Neil, T., Sommar, J., Weiss-Penzias, P., Zhang, L., and Živković, I.: Measurement of Atmospheric Mercury: Current Limitations and Suggestions for Improvements, Environ. Sci. Technol., accepted.

Hallar, A. G., Petersen, R., McCubbin, I. B., Lowenthal, D., Lee, S., Andrews, E., and Yu, F.: Climatology of New Particle Formation and Corresponding Precursors at Storm Peak Laboratory, Aerosol Air Qual. Res., 16, 816–826,
955 https://doi.org/10.4209/aaqr.2015.05.0341, 2016.

Hazard Mapping System Fire and Smoke Product: https://www.ospo.noaa.gov/Products/land/hms.html, last access: 25 October 2023.

Hopke, P. K. and Jaffe, D. A.: Letter to the Editor: Ending the Use of Obsolete Data Analysis Methods, Aerosol Air Qual. Res., 20, 688–689, https://doi.org/10.4209/aaqr.2020.01.0001, 2020.

960   Jaffe, D. A., Lyman, S., Amos, H. M., Gustin, M. S., Huang, J., Selin, N.E., Levin, L., Ter Schure, A., Mason, R. P., Talbot, R., Rutter, A., Finley, B., Jaeglé, L., Shah, V., McClure, C., Ambrose, J., Gratz, L., Lindberg, S., Weiss-Penzias, P., Sheu, G.-R., Feddersen, D., Horvat, M., Dastoor, A., Hynes, A. J., Mao, H., Sonke, J. E., Slemr, F., Fisher, J. A., Ebinghaus, R., Zhang, Y., and Edwards, G.: Progress on Understanding Atmospheric Mercury Hampered by Uncertain Measurements, Environ. Sci. Technol., 48, 7204–7206, https://doi.org/10.1021/es5026432,

965   2014.

Jolliffe, I. T. and Cadima, J.: Principal component analysis: a review and recent developments, Philosophical Transactions of the Royal Society A: Mathematical, Physical and Engineering Sciences, https://doi.org/10.1098/rsta.2015.0202, 2016.

de Krom, I., Bavius, W., Ziel, R., Efremov, E., van Meer, D., van Otterloo, P., van Andel, I., van Osselen, D.,

970   Heemskerk, M., van der Veen, A. M. H., Dexter, M. A., Corns, W. T., and Ent, H.: Primary mercury gas standard for the calibration of mercury measurements, Measurement, 169, 108351, https://doi.org/10.1016/j.measurement.2020.108351, 2021.

Lee, C. F., Elgiar, T., David, L. M., Wilmot, T. Y., Reza, M., Hirshorn, N., McCubbin, I. B., Shah, V., Lin, J. C., Lyman, S., Hallar, A. G., Gratz, L. E., and Volkamer, R.: Elevated Tropospheric Iodine over the Central Continental

975   United States: Is Iodine a Major Oxidant of Atmospheric Mercury?, Geophysical Research Letters, https://doi.org/10.22541/essoar.171136849.98199430/v1, in review.

Lin, J. C., Gerbig, C., Wofsy, S. C., Andrews, A. E., Daube, B. C., Davis, K. J., and Grainger, C. A.: A near-field tool for simulating the upstream influence of atmospheric observations: The Stochastic Time-Inverted Lagrangian Transport (STILT) model, Journal of Geophysical Research: Atmospheres, 108,

980   https://doi.org/10.1029/2002JD003161, 2003.

Liu, B., Keeler, G. J., Dvonch, J. T., Barres, J. A., Lynam, M. M., Marsik, F. J., and Morgan, J. T.: Temporal variability of mercury speciation in urban air, Atmospheric Environment, 41, 1911–1923, https://doi.org/10.1016/j.atmosenv.2006.10.063, 2007.

Loughner, C. P., Fasoli, B., Stein, A. F., and Lin, J. C.: Incorporating Features from the Stochastic Time-Inverted

985   Lagrangian Transport (STILT) Model into the Hybrid Single-Particle Lagrangian Integrated Trajectory (HYSPLIT) Model: A Unified Dispersion Model for Time-Forward and Time-Reversed Applications, Journal of Applied Meteorology and Climatology, 60, 799–810, https://doi.org/10.1175/JAMC-D-20-0158.1, 2021.

Lyman, S. N. and Jaffe, D. A.: Formation and fate of oxidized mercury in the upper troposphere and lower stratosphere, Nature Geosci, 5, 114–117, https://doi.org/10.1038/ngeo1353, 2012.

990 Lyman, S. N., Jaffe, D. A., and Gustin, M. S.: Release of mercury halides from KCl denuders in the presence of ozone, Atmospheric Chemistry and Physics, 10, 8197–8204, https://doi.org/10.5194/acp-10-8197-2010, 2010.

Lyman, S. N., Cheng, I., Gratz, L. E., Weiss-Penzias, P., and Zhang, L.: An updated review of atmospheric mercury, Science of The Total Environment, 707, 135–575, https://doi.org/10.1016/j.scitotenv.2019.135575, 2020a.

Lyman, S. N., Gratz, L. E., Dunham-Cheatham, S. M., Gustin, M. S., and Luippold, A.: Improvements to the
995 Accuracy of Atmospheric Oxidized Mercury Measurements, Environ. Sci. Technol., 54, 13379–13388, https://doi.org/10.1021/acs.est.0c02747, 2020b.

Lynam, M. M. and Keeler, G. J.: Source-receptor relationships for atmospheric mercury in urban Detroit, Michigan, Atmospheric Environment, 40, 3144–3155, https://doi.org/10.1016/j.atmosenv.2006.01.026, 2006.

Mao, H., Cheng, I., and Zhang, L.: Current understanding of the driving mechanisms for spatiotemporal variations
1000 of atmospheric speciated mercury: a review, Atmos. Chem. Phys., 16, 12897–12924, https://doi.org/10.5194/acp-16-12897-2016, 2016.

McLagan, D. S., Stupple, G. W., Darlington, A., Hayden, K., and Steffen, A.: Where there is smoke there is mercury: Assessing boreal forest fire mercury emissions using aircraft and highlighting uncertainties associated with upscaling emissions estimates, Atmos. Chem. Phys., 21, 5635–5653, https://doi.org/10.5194/acp-21-5635-2021,
1005 2021.

Miller, M. B., Dunham-Cheatham, S. M., Gustin, M. S., and Edwards, G. C.: Evaluation of cation exchange membrane performance under exposure to high Hg^0 and $HgBr_2$ concentrations, Atmospheric Measurement Techniques, 12, 1207–1217, https://doi.org/10.5194/amt-12-1207-2019, 2019.

Monks, P., Salisbury, G., Holland, G., Penkett, S. A., and Ayers, G. P.: A seasonal comparison of ozone
1010 photochemistry in the remote marine boundary layer, Atmospheric Environment, 34, 2547–2561, https://doi.org/10.1016/S1352-2310(99)00504-X, 2000.

Mueller, S. F.: Characterization of Ambient Ozone Levels in the Great Smoky Mountains National Park, Journal of Applied Meteorology and Climatology, 33, 465–472, https://doi.org/10.1175/1520-0450(1994)033<0465:COAOLI>2.0.CO;2, 1994.

1015 NOAA Air Resources Laboratory: Gridded Meteorological Data Archives: https://www.ready.noaa.gov/archives.php, last access: 20 March 2024.

Obrist, D., Moosmüller, H., Schürmann. R., Antony Chen, L.-W., and Kreidenweis, S. M.: Particulate-Phase and Gaseous Elemental Mercury Emissions During Biomass Combustion: Controlling Factors and Correlation with Particulate Matter Emissions, Environ. Sci. Technol., 42, 3, 721–727, https://doi.org/10.1021/es071279n, 2007.

1020 Obrist, D., Hallar, A. G., McCubbin, I., Stephens, B. B., and Rahn, T.: Atmospheric mercury concentrations at Storm Peak Laboratory in the Rocky Mountains: Evidence for long-range transport from Asia, boundary layer contributions, and plant mercury uptake, Atmospheric Environment, 42, 7579–7589, https://doi.org/10.1016/j.atmosenv.2008.06.051, 2008.

Obrist, D., Kirk, J. L., Zhang, L., Sunderland, E. M., Jiskra, M., and Selin, N. E.: A review of global environmental
1025 mercury processes in response to human and natural perturbations: Changes of emissions, climate, and land use, Ambio, 47, 116–140, https://doi.org/10.1007/s13280-017-1004-9, 2018.

Osterwalder, S., Nerentorp, M., Zhu, W., Jiskra, M., Nilsson, E., Nilsson, M. B., Rutgersson, A., Soerensen, A. L., Sommar, J., Wallin, M. B., Wängberg, I., and Bishop, K.: Critical Observations of Gaseous Elemental Mercury Air-Sea Exchange, Global Biogeochemical Cycles, 35, e2020GB006742, https://doi.org/10.1029/2020GB006742, 2021.

1030 Peng, Y., Mouat, A. P., Hu, Y., Li, M., McDonald, B. C., and Kaiser, J.: Source appointment of volatile organic compounds and evaluation of anthropogenic monoterpene emission estimates in Atlanta, Georgia, Atmospheric Environment, 288, 119324, https://doi.org/10.1016/j.atmosenv.2022.119324, 2022.

Saiz-Lopez, A., Acuña, A. U., Mahajan, A. S., Dávalos, J. Z., Feng, W., Roca-Sanjuán, D., Carmona-García, J., Cuevas, C. A., Kinnison, D. E., Gomez Martín, J. C., Francisco, J. S., and Plane, J. M. C.: The Chemistry of
1035 Mercury in the Stratosphere, Geophysical Research Letters, 49, https://doi. org/10.1029/2022GL097953, 2022.

Selin, N. E.: Global Biogeochemical Cycling of Mercury: A Review, Annu. Rev. Environ. Resour., 34, 43–63, https://doi.org/10.1146/annurev.environ.051308.084314, 2009.

Shah, V., Jaeglé, L., Gratz, L. E., Ambrose, J. L., Jaffe, D. A., Selin, N. E., Song, S., Campos, T. L., Flocke, F. M., Reeves, M., Stechman, D., Stell, M., Festa, J., Stutz, J., Weinheimer, A. J., Knapp, D. J., Montzka, D. D., Tyndall,
1040 G. S., Apel, E. C., Hornbrook, R. S., Hills, A. J., Riemer, D. D., Blake, N. J., Cantrell, C. A., and Mauldin III, R. L.: Origin of oxidized mercury in the summertime free troposphere over the southeastern US, Atmos. Chem. Phys, 16, 1511–1530, https://doi.org/10.5194/acp-16-1511-2016, 2016.

Shah, V., Jacob, D. J., Thackray, C. P., Wang, X., Sunderland, E. M., Dibble, T. S., Saiz-Lopez, A., Černušák, I., Kellö, V., Castro, P. J., Wu, R., and Wang, C.: Improved Mechanistic Model of the Atmospheric Redox Chemistry
1045 of Mercury, Environ. Sci. Technol., 55, 14445–14456, https://doi.org/10.1021/acs.est.1c03160, 2021.

Sheu, G.-R., Lin, N.-H., Wang, J.-L., Lee, C.-T., Ou Yang, C.-F., and Wang, S.-H.: Temporal distribution and potential sources of atmospheric mercury measured at a high-elevation background station in Taiwan, Atmospheric Environment, 44, 2393–2400, https://doi.org/10.1016/j.atmosenv.2010.04.009, 2010.

1050 Slemr, F., Brunke, E.-G., Ebinghaus, R., and Kuss, J.: Worldwide trend of atmospheric mercury since 1995, Atmos. Chem. Phys., 11, 4779–4787, https://doi.org/10.5194/acp-11-4779-2011, 2011.

Sonke, J. E., Angot, H., Zhang, Y., Poulain, A., Björn, E., and Schartup, A.: Global change effects on biogeochemical mercury cycling, Ambio, 52, 853–876, https://doi.org/10.1007/s13280-023-01855-y, 2023.

Sprovieri, F., Pirrone, N., Bencardino, M., D'Amore, F., Carbone, F., Cinnirella, S., Mannarino, V., Landis, M., Ebinghaus, R., Weigelt, A., Brunke, E.-G., Labuschagne, C., Martin, L., Munthe, J., Wängberg, I., Artaxo, P.,
1055 Morais, F., Barbosa, H. D. M. J., Brito, J., Cairns, W., Barbante, C., Diéguez, M. D. C., Garcia, P. E., Dommergue, A., Angot, H., Magand, O., Skov, H., Horvat, M., Kotnik, J., Read, K. A., Neves, L. M., Gawlik, B. M., Sena, F., Mashyanov, N., Obolkin, V., Wip, D., Feng, X. B., Zhang, H., Fu, X., Ramachandran, R., Cossa, D., Knoery, J., Maruszczak, N., Nerentorp, M., and Norstrom, C.: Atmospheric mercury concentrations observed at ground-based monitoring sites globally distributed in the framework of the GMOS network, Atmos. Chem. Phys., 16, 11915–
1060 11935, https://doi.org/10.5194/acp-16-11915-2016, 2016.

Steffen, A., Douglas, T., Amyot, M., Ariya, P., Aspmo, K., Berg, T., Bottenheim, J., Brooks, S., Cobbett, F., Dastoor, A., Dommergue, A., Ebinghaus, R., Ferrari, C., Gardfeldt, K., Goodsite, M. E., Lean, D., Poulain, A. J., Scherz, C., Skov, H., Sommar, J., and Temme, C.: A synthesis of atmospheric mercury depletion event chemistry in the atmosphere and snow, Atmos. Chem. Phys., 8, 1445–1482, https://doi.org/10.5194/acp-8-1445-2008, 2008.

1065 Swartzendruber, P. C., Jaffe, D. A., Prestbo, E. M., Weiss-Penzias, P., Selin, N. E., Park, R., Jacob, D. J., Strode, S., and Jaeglé, L.: Observations of reactive gaseous mercury in the free troposphere at the Mount Bachelor Observatory, J. Geophys. Res., 111, 2006JD007415, https://doi.org/10.1029/2006JD007415, 2006.

Timonen, H., Ambrose, J. L., and Jaffe, D. A.: Oxidation of elemental Hg in anthropogenic and marine airmasses, Atmos. Chem. Phys., 13, 2827–2836, https://doi.org/10.5194/acp-13-2827-2013, 2013.

1070 Tokarek, T. W., Odame-Ankrah, C. A., Huo, J. A., McLaren, R., Lee, A. K. Y., Adam, M. G., Willis, M. D., Abbatt, J. P. D., Mihele, C., Darlington, A., Mittermeier, R. L., Strawbridge, K., Hayden, K. L., Olfert, J. S., Schnitzler, E. G., Brownsey, D. K., Assad, F. V., Wentworth, G. R., Tevlin, A. G., Worthy, D. E. J., Li, S.-M., Liggio, J., Brook, J. R., and Osthoff, H. D.: Principal component analysis of summertime ground site measurements in the Athabasca oil sands with a focus on analytically unresolved intermediate-volatility organic compounds, Atmos. Chem. Phys., 18,
1075 17819–17841, https://doi.org/10.5194/acp-18-17819-2018, 2018.

Weigelt, A., Ebinghaus, R., Manning, A. J., Derwent, R. G., Simmonds, P. G., Spain, T. G., Jennings, S. G., and Slemr, F.: Analysis and interpretation of 18 years of mercury observations since 1996 at Mace Head, Ireland, Atmospheric Environment, 100, 85–93, https://doi.org/10.1016/j.atmosenv.2014.10.050, 2015.

Weiss-Penzias, P., Amos, H. M., Selin, N. E., Gustin, M. S., Jaffe, D. A., Obrist, D., Sheu, G.-R., and Giang, A.:
1080 Use of a global model to understand speciated atmospheric mercury observations at five high-elevation sites, Atmos. Chem. Phys., 15, 1161–1173, https://doi.org/10.5194/acp-15-1161-2015, 2015.

Xu, Z., Chen, L., Zhang, Y., Han, G., Chen, Q., Chu, Z., Zhang, Y., Li, C., Yang, Y., and Wang, X.: Meteorological Drivers of Atmospheric Mercury Seasonality in the Temperate Northern Hemisphere, Geophysical Research Letters, 49, e2022GL100120, https://doi.org/10.1029/2022GL100120, 2022.